博士論文

Investigations on intercalation cathodes for sodium-ion batteries

（ナトリウムイオン電池正極としてのインターカレーション材料の研究）

劉 貫東

Guandong Liu

Table of contents

List of Figures

List of Tables

1 Introduction

1.1 Li batteries

1.1.1 Primary Li batteries

As early as 1970s, Li batteries were firstly commercialized by several companies like Sanyo, Exxon. Those batteries are called primary Li batteries. One characteristic for this kind of battery is that it employs lithium metal as the anode material (Fig. 1.1). Under the recharge condition, Li dendrite would form on the anode surface, which might penetrate the separator and grow toward the cathode side. Consequently, short circuit will be induced and accidents happen. Thus, primary Li batteries are non-rechargeable batteries.

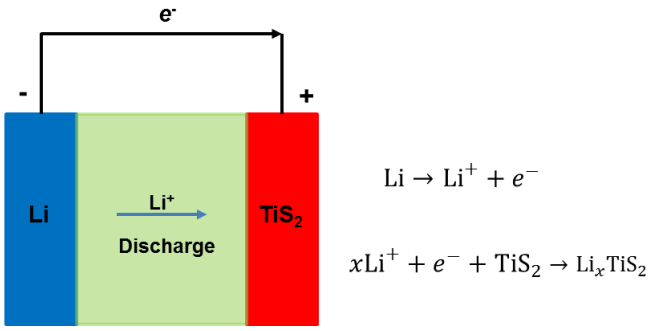

Figure 1.1 Schematic of the primary Li battery commercialize by Exxon.[1]

1.1.2 Li-ion batteries

Most Li batteries used nowadays are Li-ion batteries, which are rechargeable. In this kind of battery, the compounds that can reversibly absorb and extract Li are utilized as the anode rather than Li metal. For example, graphite is currently employed as the anode material for commercial Li-ion batteries. Li ions can be reversibly intercalated into carbon interlayers of the graphite anode during charging process, and extracted

from the interlayers in discharge process (Fig. 1.2). The reaction on the anode side can be written as

$$Li^+ + e^- + 6C \rightarrow LiC_6 \quad \text{(Charge)}$$

$$LiC_6 \rightarrow Li^+ + e^- + 6C \quad \text{(Discharge)}$$

There is no Li metal used, therefore, the formation of Li dendrite will be furthest avoided during the charge process. Consequently, the rechargeable property of the battery is reached.

To date, Li-ion batteries have been dominate in the energy storage field for portable devices, but need more efforts for the large-scale applications in electric vehicles (EV) and electric storage grid. The main problems include unsatisfied electrochemical performance, poor safety and high cost. Up to now, much work has been conducted to solve these problems.[2–7] Alternatively, through exchanging Li with Na, Na-ion batteries have re-attracted great interests for its potential to lower cost.

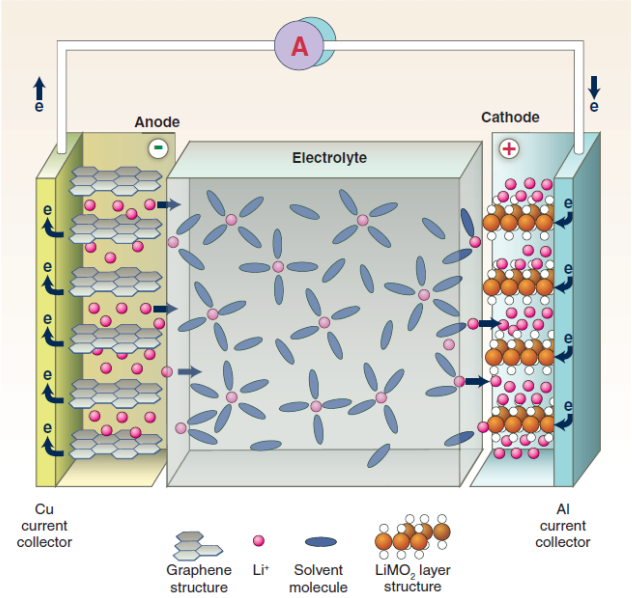

Figure 1.2 Schematic representation of a typical Li-ion battery. Derived from Technical Report of DOESC: Basic Research Needs for Electrical Energy Storage.[8]

1.2 Why Na-ion batteries

1.2.1 Natural abundance of Na

Although Li-ion batteries are widely accepted and applied in variant fields, the problem of high cost still lags their future development, especially for the large-scale application. Expensive Li resource is one of the biggest problems. As shown in Fig 1.3, there are 43.6 million tons of Li resources over the world. The reserve is enough for a maximum of 14.5 billion electric vehicles, which is about ten times the current number of automobiles.[9] However, the distribution of Li is very polarized, mostly focused in Chile, Bolivia, China, Russia, America and Canada. This uneven distribution remains the supply of Li resource a serious concern, directly inducing to the high cost of Li.

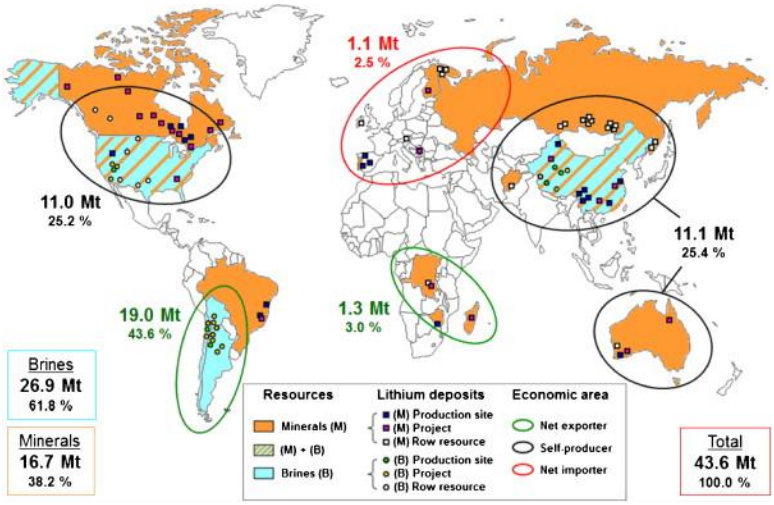

Figure 1.3 Map of lithium resource availability and geostrategic distribution, Reprinted from ref 9. Copyright (2012), with permission from Elsevier.

However, Na is one of the most abundant elements in Earth's crust. Its content is of hundreds times that of Li (Fig. 1.4), and distributed everywhere, even in the ocean. This natural abundance confirms the low cost of Na source and potentially further

induces cheap Na-ion batteries.

As early as to 1970s, Li-ion batteries and Na-ion batteries have been developed almost simultaneously. However, Li-ion batteries show higher energy density and better electrochemical performance, therefore attracted much more research interest. After the first commercialization in 1991, Li-ion batteries have become the main focus during the following two decades, with few reports on Na-ion batteries.[10] Recently, during the wide application of Li-ion batteries, the low content and uneven distribution of Li source came out to be one main concern for further application of Li-ion batteries. Na-ion batteries have re-attracted great attention mainly due to the nature abundance and low cost of Na.

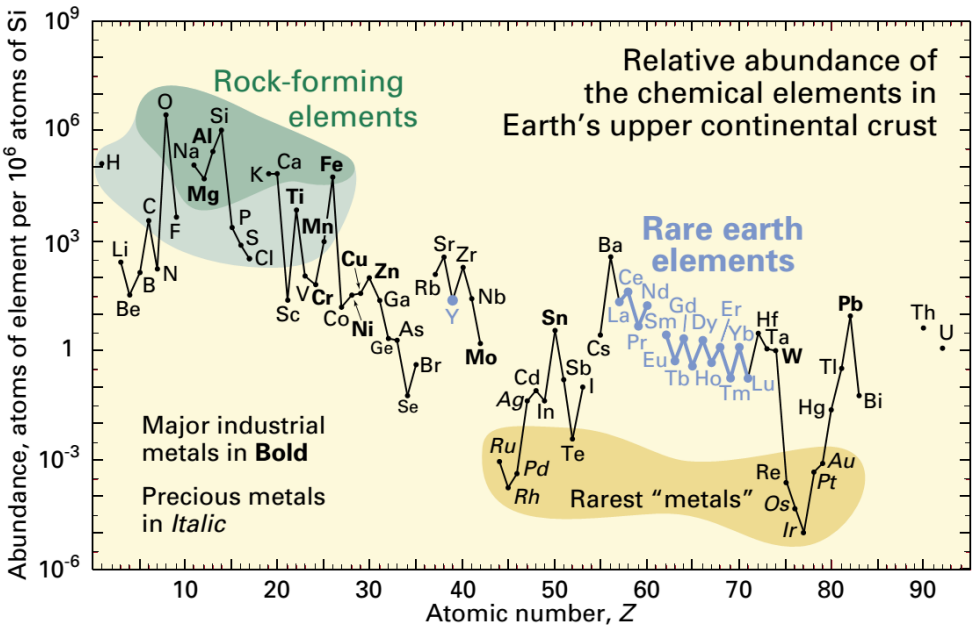

Figure 1.4 Abundance of the chemical elements in Earth's upper crust. Derived from USGS Fact Sheet 087-02 (*http://pubs.usgs.gov/fs/2002/fs087-02/fs087-02.pdf*). Courtesy of the U.S. Geological Survey.

1.2.2 Kinetic and electrochemical advantages

As shown in Fig. 1.4, besides Na, the metal elements Al, Fe, Mg, K and Ca also have abundant reserves. One decisive reason to select Na-based batteries is its kinetic advantage. Na^+ ion has better ionic conductivity in solid electrodes due to its smaller ionic size and lower valence than those of K^+, Mg^{2+}, Ca^{2+} and Al^{3+} ions. Even compared to Li^+ ion, Ceder et al[11] reported that Na ions have lower activation energies than those of Li ions for diffusion in layered transition metal oxides structure. Nakai et al[12] found that Na ion complexes generally reveal smaller de-solvation energy between the electrode/electrolyte interface than that Li ion complexes do, owing to the weaker Lewis acidity of Na ions. All these indicate the potential of high rate capability for Na-based batteries.

Table 1.1 Standard reduction potential (E_0) for selected half-cell reaction

E_0 (V)	Reduction reaction
0	$2H^+ (aq) + 2e^- \rightarrow H_2 (g)$
-0.44	$Fe^{2+} (aq) + 2e^- \rightarrow Fe (s)$
-1.66	$Al^{3+} (aq) + 3e^- \rightarrow Al (s)$
-2.38	$Mg^{2+} (aq) + 2e^- \rightarrow Mg (s)$
-2.71	$Na^+ (aq) + e^- \rightarrow Na (s)$
-2.87	$Ca^{2+} (aq) + 2e^- \rightarrow Ca (s)$
-2.94	$K^+ (aq) + e^- \rightarrow K (s)$
-3.04	$Li^+ (aq) + e^- \rightarrow Li (s)$

Besides, Na-ion batteries also show electrochemical advantages. Table 1.1 lists the standard reduction potentials for the abundant metals mentioned above. Generally, the

lower the reduction potential is, the higher the voltage of whole batteries with the metal on the anode side. Na has a low reduction potential of -2.71 V, only 0.33V higher than that of Li. Therefore, Na-ion batteries have relatively high voltages.

1.2.3 Similarity of Na-ion battery to Li-ion battery

Na-ion batteries take the similar architecture to that of Li-ion batteries. Thus, development on Na-ion batteries can be inspired by successful experiences in the research of Li-ion batteries. Both the batteries consist of three main components, cathode, anode and electrolyte

The same to those in Li-ion batteries, Na-ion batteries also mainly employ intercalation-type materials as the cathodes. Until now, many promising intercalation cathode materials for Li-ion batteries have been discovered, and their Na analogues are developed for Na-ion battery cathode materials.[13–15] These cathode materials can be divided into two main groups, transition metal oxides and polyanionic compounds, which will been introduced in detail as the next section.

As the anode material, graphite is commonly applied in commercial Li-ion batteries. It delivers a high reversible capacity near the theoretical value of 372 mAh/g. However, graphite is not suitable for Na system because Na ions cannot intercalate into the carbon interlayers generally. Although a reversible capacity for graphite was reported in diglyme-based electrolyte due to co-intercalation of Na ion and dilgyme,[16] the capacity of ca. 100 mAh/g is relatively less than that in Li system.

Hard carbon is the artificial carbon with disordered array of graphite crystallites, and cannot be graphitized by high temperature treatment at ca. 3000 K. Generally, hard carbon is more stable, and was used in commercial Li-ion batteries originally. However,

the low volumetric capacity due to the low density limits its application, and therefore it was replaced by graphite soon in 1990s. In Na-ion battery system, Stevens and Dahn reported the reversible intercalation/de-intercalation of Na in hard carbon at room temperature with a high capacity of ca. 300 mAh/g,[17] proving hard carbon is much more promising than graphite as the anode material for Na-ion batteries.

Besides, Na alloy electrode materials are also widely investigated. Tin, Antimony and lead have been demonstrated with high capacity. However, volume change of alloys during the absorption/extraction of Na is generally twice in extent to that of Li system.[18,19] This fact leads to the serious cracking of anode materials during electrochemical cycling and results in capacity loss.

In the common Li-ion batteries, lithium salts dissolved in carbonate ester solvents have been widely utilized mainly due to that carbonate esters have high ionic conductivity, wide potential window, low toxicity et al.[20] Carbonate ester solvents containing sodium salts are expected to be good electrolyte for Na-ion batteries. Palacín et al investigated the performance of various electrolyte solutions with different Na salts and carbonate ester solvents in Na/hard carbon cells.[21] The binary solvent mixture of ethylene carbonate (EC) and propylene carbonate (PC) has emerged at the best choice with $NaClO_4$ or $NaPF_6$ as the dissolved salt. However, the binary mixture of ethylene carbonate (EC) and diethyl carbonate (DEC), a conventional solvent in commercial Li electrolyte, was demonstrated unsuitable for Na system. Obvious capacity decline occurs within a few initial cycles.

Consequently, Na-ion batteries have been largely developed with the experiences in Li-ion batteries investigation, based on the similarity of the two types of batteries. However, also many differences have been observed between the two systems,

therefore efforts on independent research of Na-ion batteries are urgent for their practical application in the near future. Besides, Na-ion batteries are only alternative for large-scale applications where low cost is more important, due to that Na-ion batteries may not match the energy density of Li-ion batteries because the heavier weight (23 g/mol) and lower oxidation potential (2.71 V) of Na, compared to those (6.9 g/mol, 3.04 V) of Li.

1.3 Intercalation cathode materials for Na-ion batteries

In 1970s, layered transition metal dichalcogenides MX_2 were found to be intercalated by alkali metal atoms without obvious structure change.[22] As an example, the intercalation of Li in TiS_2 is shown in Fig 1.5. Li ions could be intercalated into the interlayers between the two adjacent TiS_2 layers. As-formed Li_xTiS_2 keeps the original layered structure with an alternate stacking of TiS_2 layer and Li layer, and can reversibly extract the intercalated Li ions to change back to TiS_2. In light of the Li_xTiS_2 research, intercalation of Na in TiS_2 has also been conducted at almost the same time.[23] And the name "intercalation compounds" was introduced.

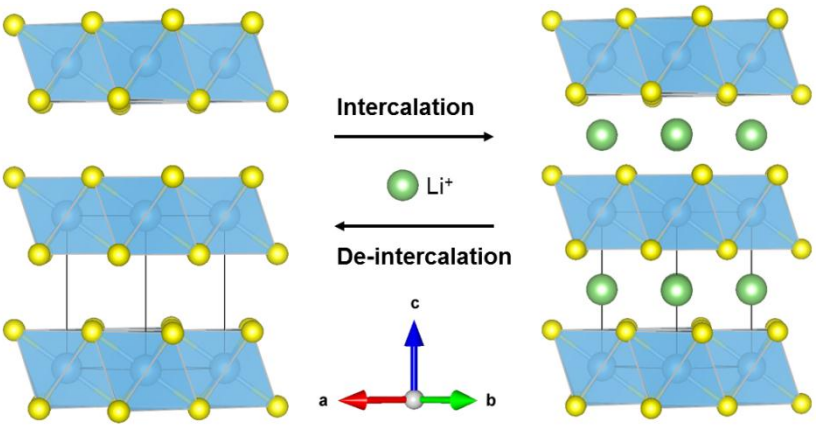

Figure 1.5 Schematic representation of intercalation process in TiS_2. Ti (blue) atoms are located in the octahedral site surrounded by six S (yellow) atoms.

1.3.1 Transition metal oxides

1.3.1.1 Characteristics

As transition metal dichalgenides always show low redox potentials, researchers turned their focus on oxides. In the field of Li-ion battery research, numerous lithium transition metals oxides have been developed as promising intercalation electrodes, i.e. layered $LiCoO_2$ and spinel $LiMn_2O_4$, which have been already widely applied in the practical applications. Inspired by the success of transition metal oxides in the Li-ion battery field, the similar formula compounds Na*TM*O_2 (*TM* = transition metals) are considered as potential electrode materials for Na-ion batteries.

As a typical characteristic, Na*TM*O_2 compounds take only "simple" oxygen lattice, without other non-metal elements like P in phosphates or S in sulfates. Therefore, they always have smaller molecular weights and higher theoretic specific capacities as electrode materials. This is one main advantage for Na*TM*O_2-type cathode materials. However simultaneously, Na*TM*O_2 have weaker *TM*-O bonds, and therefore less stable crystal structures comparing to polyanionic compounds.

1.3.1.2 Layered oxides

Similar to the structure of Li_xTiS_2 as shown in Fig. 1.5, layered lithium transition metal oxides commonly consist of two alternate layers, transition metal layer and lithium layer. The structures can also be recognized as a stacking of oxygen layers with sodium and transition metal atoms occupying the inside vacancies. Based on the different series of stacking of oxygen layers, O3- (ABCABC) and P2- (ABBA) type structures have be defined as shown in Fig1.6. In the O3-type structure, the stack period

of oxygen layers (or slabs) is 3 (ABC), and Na atoms intercalate in the interlayers where different kinds of oxygen slabs on the upper and bottom sides, therefore are located in octahedral sites. On the other hand, prismatic polyhedrons are formed for NaO_6 in the P-type structure. As shown in the right of Fig. 1.6, P2-type is called due to the prismatic NaO_6 polyhedra and the stacking period of 2 (AB).

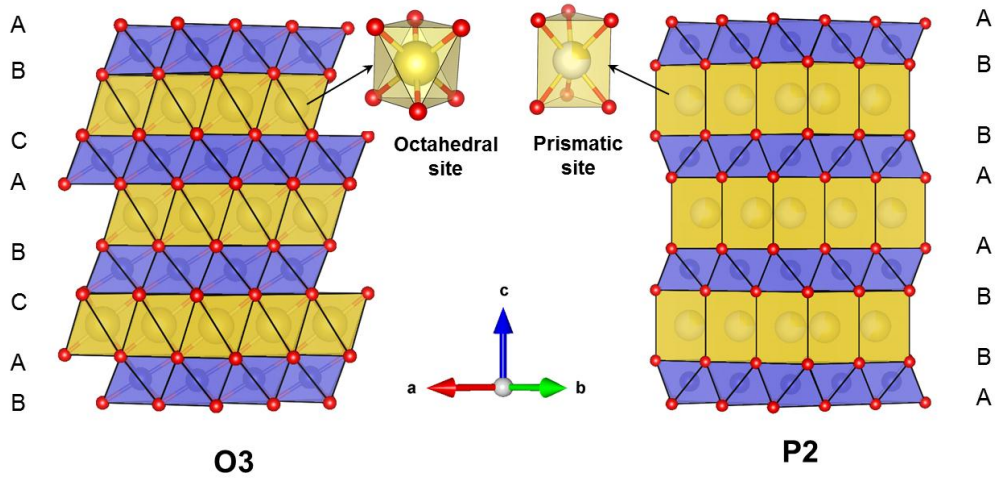

Figure 1.6 Schematic representation of O3- and P2-type layered structures.

Many layered sodium transition metal oxides with O3- and P2-type structures have been developed as the cathode materials for Na-ion batteries. Their reversible capacities and operating voltages can be checked from Fig 1.7 reported by Komaba et al.[24] Although the theoretic specific capacities of this series of oxides are much high (e.g. 235 mAh/g for $NaCoO_2$), the practical reversible values are not so attractive. O3-type $NaFeO_2$,[25] $NaCrO_2$[26] and $NaCoO_2$[27] only show the specific capacities of ca. 100 mAh/g.

As an exception, P2-$Na_{2/3}(Fe_{1/2}Mn_{1/2})O_2$ delivers a high reversible capacity of 190 mAh/g with an average voltage of 2.75 V.[24] However, three main disadvantages have been reported,[20] including a large volume change during electrochemical cycles, hygroscopic property and additional efforts needed for full-cell assembly due to the Na

deficiency.

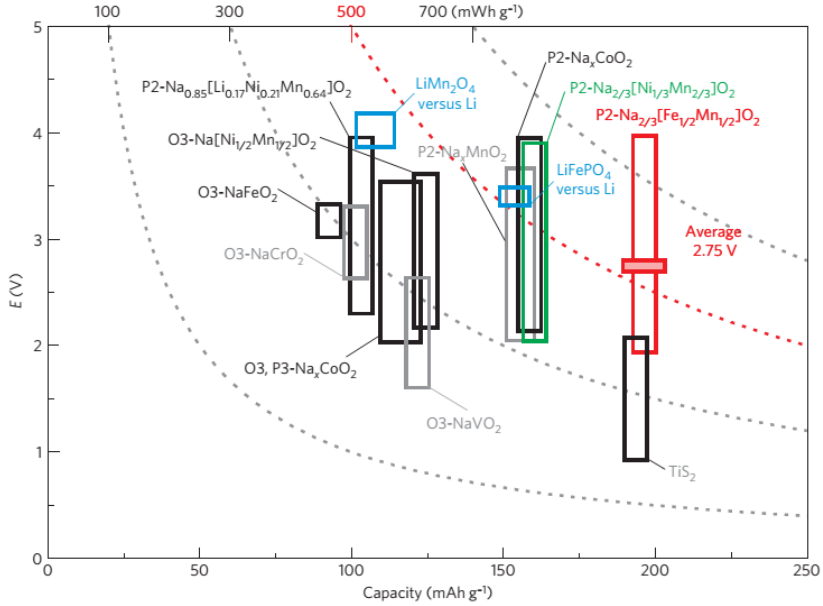

Figure 1.7 A comparison of reversible capacity and operating voltage (*versus* Na/Na^+) of layered sodium transition metal oxides. $LiFePO_4$ and $LiMn_2O_4$ are depicted for comparison with Li ion batteries, their operating voltages are calculated versus Li/Li^+ electrode. Reprinted by permission from Macmillan Publishers Ltd: [Nature Materials] (ref 24), copyright (2012).

1.3.1.3 Tunnel-type oxides

Unlike $LiMnO_2$, 50% desodiation of $NaMnO_2$ does not result in a layered – spinel structure transformation (layered $LiMnO_2$ → spinel $Li_{0.5}MnO_2$ ($LiMn_2O_4$)). A phase of $Na_{0.44}MnO_2$ with tunnels suitable for Na incorporation has be identified.[28]

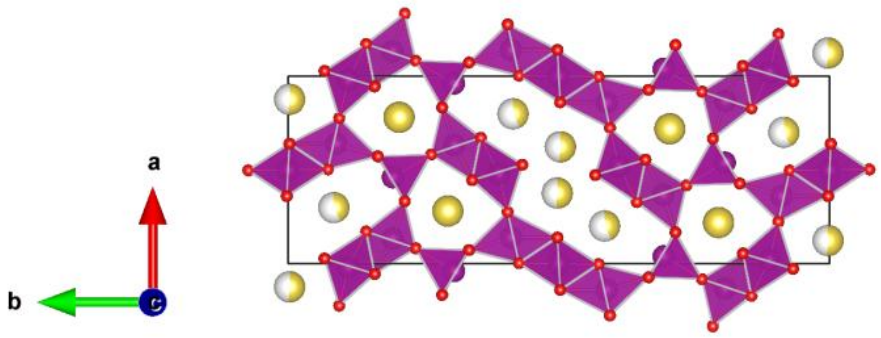

Figure 1.8 Crystal structure of tunnel-type $Na_{0.44}MnO_2$. Na, Mn and O atoms are depicted as yellow, purple and red balls, respectively.

As shown in Fig. 1.8, $Na_{0.44}MnO_2$ crystallizes in an orthorhombic symmetry (space group: *Pbam*). Mn atoms are located in octahedral (MnO_6) or square-pyramidal (MnO_5) sites. They surround two kinds of Na tunnels parallel to the *c* direction. In detail, a larger tunnel with S shape contains four half-filled Na sites, and a smaller tunnel with only one fully filled Na site. Baudrin et al[29] studied the intercalation/de-intercalation of Na in $Na_{0.44}MnO_2$. At very slow rate (C/200), a specific capacity of 140 mAh/g was obtained in the voltage range of 2-3.8 V. However, the capacity fallen down to ~80 mAh/g with a higher rate (C/10) and ~30 mAh/g after 45 cycles.

1.3.2 Polyanionic compounds

Besides the transition metal oxides, the other group of cathode material for Na-ion batteries belongs to polyanion-based compounds, like phosphates, sulfates. At the expense of higher molecular weight and therefore lower specific capacity, polyanionic compounds gain three main advantages described as below.

1.3.2.1 Inductive effect

The inductive effect was first introduced by Goodenough et al[30,31] to explain the voltage shift of Fe^{3+}/ Fe^{2+} in $Fe_2(MO_4)_3$ (M = W, Mo, S) compounds. The OCV of $Fe_2(SO_4)_3$ is 3.6 V *versus* Li metal, 600 mV higher than that of $Fe_2(WO_4)_3$ and $Fe_2(MoO_4)_3$, even that these compounds possess the similar Fe-O bond lengths and same charge state of Fe ion. Goodenough et al explained the phenomenon with inductive effect. The inductive effect of *M* along Fe-O-*M* linkage pulls electrons away from Fe ions, and increases the ionic character of Fe-O bonds. This effect decreases the Fermi level of $Li_xFe_2(MO_4)_3$, consequently results in a higher OCV *versus* Li metal. The higher the electronegativity of *M*, the stronger the inductive effect, and therefore the more the OCV increment. Consequently, the differential of 600 mV in OCV of $Fe_2(MO_4)_3$ is mainly resulted from the higher electronegativity of S, comparing to that of W, or Mo.

Inductive effect has been widely used to understand the voltage shift in polyanionic electrode materials.[14] It also points one direction to design high-voltage electrode materials — through increasing the electronegativity of polyanions. As a result, many fluorosulphates,[32,33] fluorophosphates,[34,35] and pyrophosphates[36–39] compounds have been investigated due to the high electronegativity of their polyanions (SO_4F^{3-}, PO_4F^{4-}, $P_2O_7^{4-}$).

1.3.2.2 Stable structural framework

Compared to oxides, polyanionic compounds show much more stable structure frameworks because of the stable polyanion groups, *i.e.* PO_4^{3-}, SO_4^{2-} et al. Higher covalent bonding energy in polyanions stabilizes the oxygen stack and provides the

stable crystal structures. These stable frameworks give the potential of high reversibility and safety as electrode materials.

1.3.2.3 Rich crystallography

Polyanionic compounds show very rich crystallography, which can be used to optimize the ionic/electric conductivities and to search excellent alters for cathode materials of Na-ion batteries. Typical structure models include Olivine, NASICON, layered, Alluaudite, Titanite types and a triclinic phase for $Na_2MP_2O_7$ (M= Fe, Mn).[40] The detailed crystal structures of typical compounds are illustrated in Fig. 1.9. Table 1.2 lists their electrochemical performance as cathode materials in Na-ion batteries.

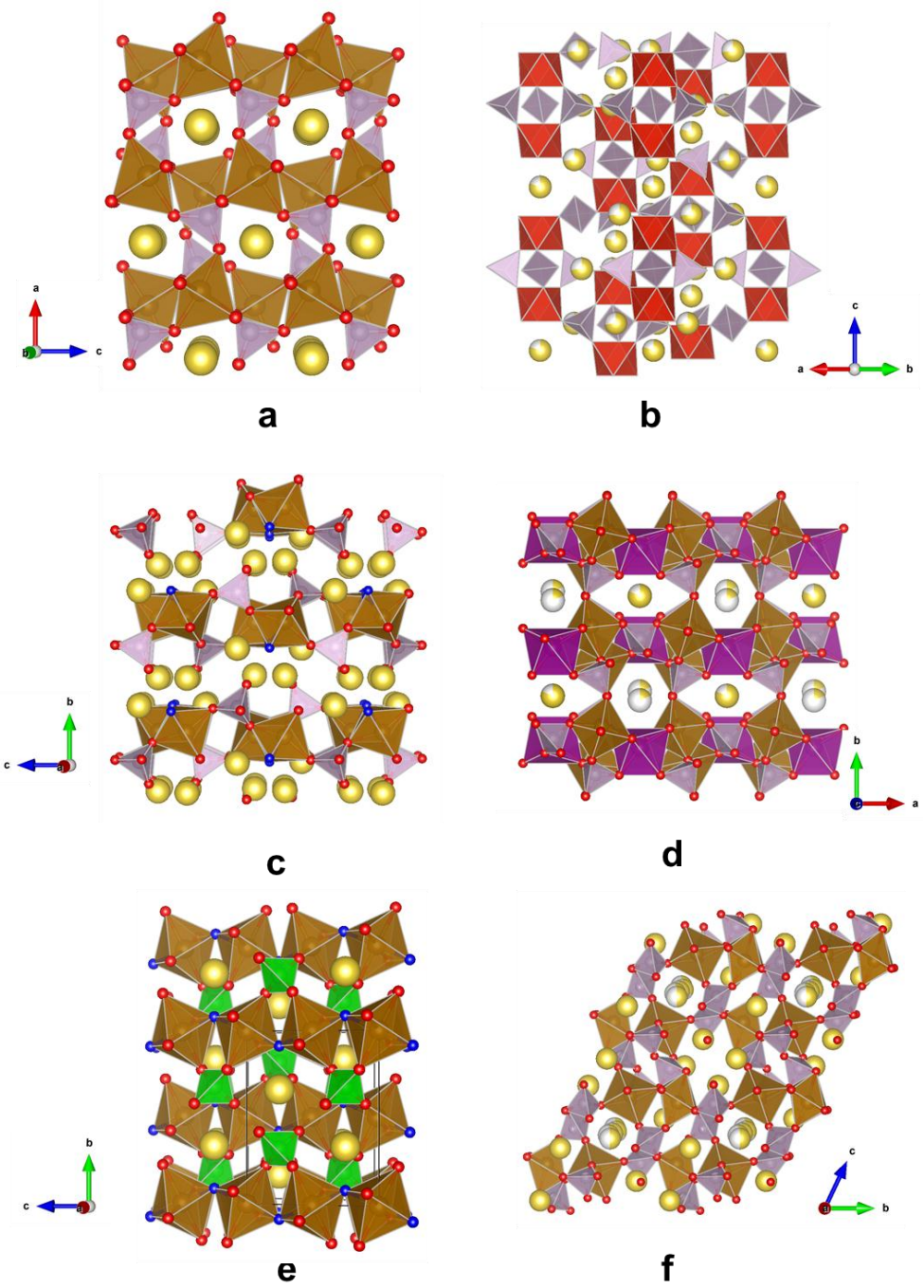

Figure 1.9 Crystal structure illustration of Olivine $NaFePO_4$ (a), NASICON $Na_3V_2(PO_4)_3$ (b), Layered Na_2FePO_4F (c), Alluaudite $NaMnFe_2(PO_4)_3$ (d), Titanite $Na_2Fe(SO_4)F$ (e) and triclinic $Na_2FeP_2O_7$ (f). Na, Fe, Mn, V, P, S and F atoms are depicted as yellow, brown, purple, reddish-brown, lavender, green and blue balls, respectively.

Table 1.2 A comparison of electrochemical performance of selected polyanion-based cathode materials for Na-ion batteries.

Structure type	Cathode materials	Redox couple	Average potential (V) versus Na/Na^+	Theoretic capacity (mAh/g)	Reference
Olivine	$NaFePO_4$	Fe^{3+}/Fe^{2+}	~2.8	154	[41]
NASICON	$Na_3V_2(PO_4)_3$	V^{4+}/V^{3+}	~3.4	118	[42]
Layered	Na_2FePO_4F	Fe^{3+}/Fe^{2+}	~3.0	124	[43]
Alluaudite	$NaMnFe_2(PO_4)_3$	Fe^{3+}/Fe^{2+} Mn^{3+}/Mn^{2+}	~3.0	148	[44]
Titanite	$NaFeSO_4F$	Fe^{3+}/Fe^{2+}	~3.6	138	[33]
Triclinic	$Na_2FeP_2O_7$	Fe^{3+}/Fe^{2+}	~3.0	97	[36,38]

1.4 Motivation and purpose

Because of the low cost and natural abundance of Na, Na-ion batteries are considered to be suitable for large-scale application to instead of Li-ion batteries. However currently, Na-ion batteries are still far from the practical application due to the unsatisfied electrochemical performance and safety issue. More efforts are compelling.

My thesis focuses on the research of cathode materials for Na-ion batteries and mainly includes two parts. The first part investigates polyanoinic $Na_{2-x}M_{1+x/2}P_2O_7$-type (M = Fe, Mn, Mg…) compounds. Chapter 3 will describe the safety issue in $Na_2FeP_2O_7$, which is considered as a potential cathode material for Na-ion batteries.[36,38] Chapter 4

will concentrate on the ionic conduction mechanism in the $Na_{2-x}M_{1+x/2}P_2O_7$-type structure. As the redox activity of transition metal would introduce undesirable defects and affect the as-measured conduction properties, a transition metal free analogue, $Na_{1.82}Mg_{1.08}P_2O_7$, is chosen as a model system. In chapter 5, a new phase of layered $Na[Na_{1/3}Ru_{2/3}]O_2$ oxide with honeycomb ordering on the $Na_{1/3}Ru_{2/3}$ slab will be introduced as an alternative cathode material with high capacity and good rate capability.

1.5 Reference

(1) Whittingham, M. *Science*. **1976**, *192*, 1126–1127.

(2) Whittingham, M. S. *Chem. Rev.* **2004**, *104*, 4271–4301.

(3) Goodenough, J. B.; Kim, Y. *Chem. Mater.* **2010**, *22*, 587–603.

(4) Dunn, B.; Kamath, H.; Tarascon, J.-M. *Science.* **2011**, *334*, 928–935.

(5) Girishkumar, G.; Mccloskey, B.; Luntz, A. C.; Swanson, S.; Wilcke, W. **2010**, 2193–2203.

(6) Ceder, G.; Chiang, Y.; Sadoway, D. *Nature* **1998**, *392*, 694–696.

(7) Curtarolo, S.; Hart, G. L. W.; Nardelli, M. B.; Mingo, N.; Sanvito, S.; Levy, O. *Nat. Mater.* **2013**, *12*, 191–201.

(8) Goodenough, J.; Abruña, H.; Buchanan, M. *Basic research needs for electrical energy storage (Washington, D.C.: Office of Basic Energy Science, U.S. Department of Energy)*; 2007.

(9) Grosjean, C.; Miranda, P. H.; Perrin, M.; Poggi, P. *Renew. Sustain. Energy Rev.* **2012**, *16*, 1735–1744.

(10) Han, M. H.; Gonzalo, E.; Singh, G.; Rojo, T. *Energy Environ. Sci.* **2014**, Accepted Manuscript, DOI: 10.1039/C4EE03192J.

(11) Ong, S. P.; Chevrier, V. L.; Hautier, G.; Jain, A.; Moore, C.; Kim, S.; Ma, X.; Ceder, G. *Energy Environ. Sci.* **2011**, *4*, 3680–3688.

(12) Okoshi, M.; Yamada, Y.; Yamada, a.; Nakai, H. *J. Electrochem. Soc.* **2013**, *160*, A2160–A2165.

(13) Palomares, V.; Serras, P.; Villaluenga, I.; Hueso, K. B.; Carretero-González, J.; Rojo, T. *Energy Environ. Sci.* **2012**, *5*, 5884.

(14) Masquelier, C.; Croguennec, L. *Chem. Rev.* **2013**, *113*, 6552–6591.

(15) Ellis, B. L.; Nazar, L. F. *Curr. Opin. Solid State Mater. Sci.* **2012**, *16*, 168–177.

(16) Jache, B.; Adelhelm, P. *Angew. Chem. Int. Ed. Engl.* **2014**, *53*, 10169–10173.

(17) Stevens, D. a.; Dahn, J. R. *J. Electrochem. Soc.* **2000**, *147*, 1271.

(18) Liu, N.; Lu, Z.; Zhao, J.; McDowell, M. T.; Lee, H.-W.; Zhao, W.; Cui, Y. *Nat. Nanotechnol.* **2014**, *9*, 187–92.

(19) Chevrier, V. L.; Ceder, G. *J. Electrochem. Soc.* **2011**, *158*, A1011.

(20) Yabuuchi, N.; Kubota, K.; Dahbi, M.; Komaba, S. *Chem. Rev.* **2014**, *114*, 11636–11682.

(21) Ponrouch, A.; Marchante, E.; Courty, M.; Tarascon, J.-M.; Palacín, M. R. *Energy Environ. Sci.* **2012**, *5*, 8572.

(22) Gamble, F.; Osiecki, J.; Cais, M. *Science.* **1971**, 493–497.

(23) Silbernagel, B. G.; Whittingham, M. S. *Mater. Res. Bull.* **1976**, *11*, 29–36.

(24) Yabuuchi, N.; Kajiyama, M.; Iwatate, J.; Nishikawa, H.; Hitomi, S.; Okuyama, R.; Usui, R.; Yamada, Y.; Komaba, S. *Nat. Mater.* **2012**, *11*, 512–517.

(25) Yabuuchi, N.; Yoshida, H.; Komaba, S. *Electrochemistry* **2012**, *80*, 716–719.

(26) Komaba, S.; Takei, C.; Nakayama, T.; Ogata, A.; Yabuuchi, N. *Electrochem. commun.* **2010**, *12*, 355–358.

(27) Delmas, C.; Braconnier, J.; Fouassier, C.; Hagenmuller, P. *Solid State Ionics* **1981**, *3/4*, 165–169.

(28) Doeff, M. M.; Richardson, T. J.; Kepley, L. *J. Electrochem. Soc.* **1996**, *143*, 2507–2516.

(29) Sauvage, F.; Laffont, L.; Tarascon, J.-M.; Baudrin, E. *Inorg. Chem.* **2007**, *46*, 3289–3294.

(30) Manthiram, A.; Goodenough, J. B. *J. Power Sources* **1989**, *26*, 403–408.

(31) Manthiram, A.; Goodenough, J. B. *J. Solid State Chem.* **1987**, *71*, 349–360.

(32) Tripathi, R.; Gardiner, G. *Chem. Mater.* **2011**, *23*, 2278–2284.

(33) Barpanda, P.; Chotard, J.-N.; Recham, N.; Delacourt, C.; Ati, M.; Dupont, L.; Armand, M.; Tarascon, J.-M. *Inorg. Chem.* **2010**, *49*, 7401–7413.

(34) Serras, P.; Palomares, V.; Goñi, A.; Gil de Muro, I.; Kubiak, P.; Lezama, L.; Rojo, T. *J. Mater. Chem.* **2012**, *22*, 22301.

(35) Barker, J.; Saidi, M. Y.; Swoyer, J. L. *Electrochem. Solid-State Lett.* **2003**, *6*, A1–A4.

(36) Kim, H.; Shakoor, R. A.; Park, C.; Lim, S. Y.; Kim, J.-S.; Jo, Y. N.; Cho, W.; Miyasaka, K.; Kahraman, R.; Jung, Y.; Choi, J. W. *Adv. Funct. Mater.* **2013**, *23*, 1147–1155.

(37) Barpanda, P.; Nishimura, S.; Yamada, A. *Adv. Energy Mater.* **2012**, *2*, 841–859.

(38) Barpanda, P.; Ye, T.; Nishimura, S.; Chung, S.-C.; Yamada, Y.; Okubo, M.; Zhou, H.; Yamada, A. *Electrochem. commun.* **2012**, *24*, 116–119.

(39) Ha, K.-H.; Woo, S. H.; Mok, D.; Choi, N.-S.; Park, Y.; Oh, S. M.; Kim, Y.; Kim, J.; Lee, J.; Nazar, L. F.; Lee, K. T. *Adv. Energy Mater.* **2013**, *3*, 770–776.

(40) Barpanda, P.; Liu, G.; Ling, C. D.; Tamaru, M.; Avdeev, M.; Chung, S.-C.; Yamada, Y.; Yamada, A. *Chem. Mater.* **2013**, *25*, 3480–3487.

(41) Zhu, Y.; Xu, Y.; Liu, Y.; Luo, C.; Wang, C. *Nanoscale* **2013**, *5*, 780–787.

(42) Plashnitsa, L. S.; Kobayashi, E.; Noguchi, Y.; Okada, S.; Yamaki, J. *J. Electrochem. Soc.* **2010**, *157*, A536–A543.

(43) Ellis, B. L.; Makahnouk, W. R. M.; Makimura, Y.; Toghill, K.; Nazar, L. F. *Nat. Mater.* **2007**, *6*, 749–753.

(44) Trad, K.; Carlier, D.; Croguennec, L.; Wattiaux, A.; Ben Amara, M.; Delmas, C. *Chem. Mater.* **2010**, *22*, 5554–5562.

2 Methods and theories

2.1 X-ray diffraction

X ray is the electromagnetic radiation with a wavelength range of 0.1~100 Å. Because this wavelength range is similar to the interplanar spacing in crystal structure, diffraction phenomenon may happen when X-ray beam incidents to the crystalline matter. As well known, Bragg's law is used to determine the situation when X-ray diffraction happens.[1]

$$2d_{hkl}\sin\theta = \lambda \qquad (2.1)$$

Where d_{hkl} is the interplanar distance, θ is the angle between incident X-ray beam and crystal plane, and λ denotes the wavelength of X ray. During this diffraction process, only elastic scattering is considered, which means, the wavelength is constant for the incident and diffracted X-ray beams.

With constant and known λ value, the interpanar spacing information in crystal structure can be deduced from the θ where X-ray diffraction happens. Plus that the detailed atomic distribution in the *hkl* plane would contributes to the diffraction intensity I_{hkl}, according to the equation

$$I_{hkl} = |F_{hkl}|^2 \qquad (2.2)$$

$$F_{hkl} = \sum_{n=1}^{N} f_n e^{-B\frac{sin^2\theta}{\lambda^2}} \times e^{2\pi i(hx_n+ky_n+lz_n)} \qquad (2.3)$$

In which F_{hkl} is called structure factor, N is the number of atoms on the *hkl* plane, f_n the atomic scatter factor, *B* the thermal factor, x_n, y_n and z_n are used to represent the atomic position of n. Consequently, the information, including interplanar spacing, atomic distribution *et al*., can be obtained from the X-ray diffraction, and then is used to deduce the fine crystal structure.

2.2 Rietveld refinement

Rietveld refinement is a technique proposed by Hugo Rietveld for the structure characterization of crystalline materials.[2] The principle is to minimize sum of the weighted, squared residuals (*WSS*) using a least squares algorithm[3]

$$WSS = \sum_i w_i (y_i^{exp} - y_i^{cal})^2 \qquad (2.4)$$

Where w_i is weighting parameter, y_i^{exp} is the intensity of diffraction peak *i* obtained from experimental XRD patterns, and y_i^{cal} is the calculated intensity according to

$$y_i^{cal} = S \sum m_{hkl} |F_{hkl}|^2 L(\theta_{hkl}) P_{hkl} G(\Delta 2\theta_{hkl}) A + bkg_i \qquad (2.5)$$

Where S is the scale factor, m_{hkl} is the multiplicity of *hkl* diffraction, F_{hkl} is the structure factor calculated according to equation (2.3). $L(\theta_{hkl})$ is the Lorentz-Polarization factor calculated as

$$L(\theta_{hkl}) = \frac{1-\mu+\mu cos^2 2\theta_M cos^2 2\theta_{hkl}}{2 sin^2 \theta_{hkl} cos\theta_{hkl}} \qquad (2.6)$$

Where θ_M denotes the Bragg angle of the monochromator, μ is a constant for specific instrumental geometry and X-ray resource. P_{hkl} in equation (2.5) represents the texture condition of sample, and *A* denotes the X-ray absorption of sample. $G(\Delta\theta_{hkl})$ is used to describe the peak profile, and its formula depends on employed profile shape function, i.e. Lorentzian, Gaussian, Voigt, Pseudo-Voigt, Pearson VII.

After Rietveld refinement, the reliability indices (*R*) are used to indicate the refinement quality. *R* indices are defined as

$$R_p = \frac{\sum_{i=1}^{N} \left| y_i^{exp} - y_i^{cal} \right|}{\sum_{i=1}^{N} y_i^{exp}} \qquad (2.7)$$

$$R_{wp} = \left[\frac{\sum_{i=1}^{N} w_i \left(y_i^{exp} - y_i^{cal} \right)^2}{\sum_{i=1}^{N} w_i (y_i^{exp})^2} \right]^{1/2} \qquad (2.8)$$

$$R_{exp} = \left[\frac{N-n}{\sum_{i=1}^{N} w_i (y_i^{exp})^2}\right]^{1/2} \qquad (2.9)$$

$$\mathrm{GOF} = \frac{R_{wp}}{R_{exp}} \qquad (2.10)$$

2.3 Mössbauer spectroscopy

As shown in Fig. 2.1, a nucleus in an excited state with energy E_e can emit a gamma photon with energy E_e-E_g, and undergoes transition to the ground state (E_g). The emitted gamma photon can be absorbed by a same kind nucleus (same number of proton and neutron) in its ground state, and induce a transition to the excited state of energy E_g. This phenomenon is called nuclear resonance absorption of gamma ray, or Mössbauer effect after Rudolf Mössbauer.[4–7]

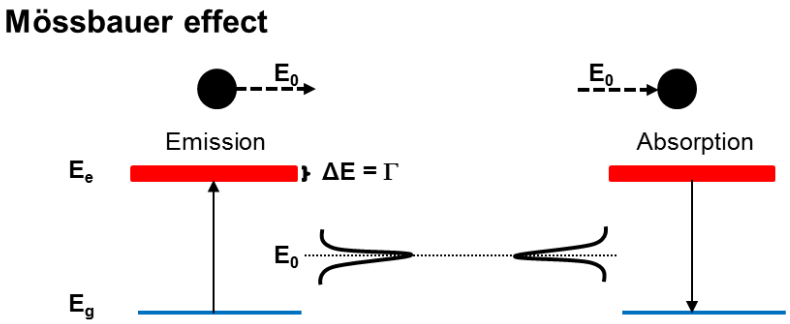

Figure 2.1 Mössbauer effect of nucleus through absorption of gamma ray, which is emitted from the identical nucleus.

The gamma ray has an extraordinarily narrow range of energy, therefore a small nature line width Γ. Using ^{57}Fe source as an example, $\Gamma = 4.7\times10^{-9}$ eV, and the energy of gamma photon E_γ = 14.4 Kev, therefore $\Gamma/E_\gamma = 3.26\times10^{-13}$, which indicates the sharpness of energy distribution range of gamma ray. Thus, a shift lager than Γ on the energy of emitted gamma ray (E_0 in Fig. 2.1) would make nuclear resonance absorption

impossible, and therefore prohibit the happen of Mössbauer effect.

This is very true when the recoil effect is considered. In the practical case, through emission or absorption of gamma photons in a free atom, a recoil phenomenon will happen and change the energy of gamma photons E_γ (Fig. 2.1). Suppose that the energy induced by the recoil effect is E_R, it can be calculated according to[8]

$$E_R = \frac{E_\gamma^2}{2mc^2} \qquad (2.11)$$

Where *m* is mass of the atom, c is light velocity. E_R is much larger than the natural width Γ, i.e. for ^{57}Fe source, $E_R = 2\times10^{-3}$ eV ≈ 10^6 Γ. Therefore, Mössbauer effect is impossible for a free atom or molecule in gas and liquid.

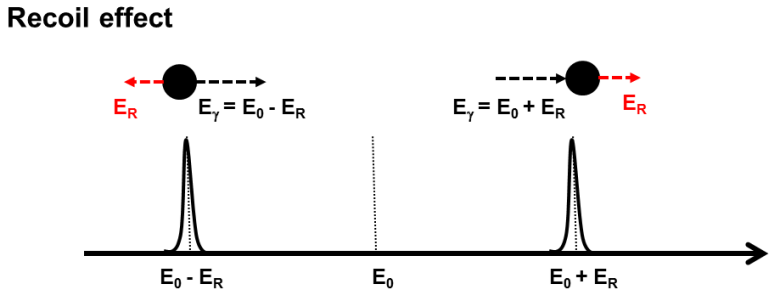

Figure 2.2 Schematic representation of recoil effect in nucleus through emission or absorption of gamma photons.

In solid crystal, atoms are located and fixed in the rigid lattice. In this case, the recoil effect refers to the whole crystal particle of mass *M* instead of an individual atom with the mass of *m*, therefore, E_R should be calculated with exchange *m* with *M* in equation (2.11). Because *M*>> *m*, E_R is much smaller than Γ. Thus, recoil effect can be ignored and Mössbauer effect becomes possible. A recoil-free fraction *f* is used to represent the fraction that recoil-free emission and absorption of gamma ray happen, i.e. *f* = 0.91 for ^{57}Fe source at room temperature.

The above considerations are based on two identical nucleuses, which is usually not the case actually. The hyperfine interaction between electric and magnetic fields of the surrounded electrons and nuclear field may slightly change the energy state of nucleus, therefore influent the Mössbauer effect. To obtain the maximum Mössbauer effect, Doppler Effect is applied in the Mössbauer spectroscopy, by moving the emission source and the absorber relative to each other. Energy differential ΔE induced by the hyperfine interaction is corrected with Doppler velocity *v* according to

$$\Delta E = \frac{v}{c} E_\gamma \qquad (2.12)$$

The hyperfine interaction includes three parts, electric monopole interaction between protons of the nucleus and electrons penetrating the nuclear field (mainly from s orbits), electric quadrupole interaction between the nuclear quadrupole moment and an inhomogeneous electric field at the nucleus, and magnetic dipole interaction between the nuclear magnetic dipole moment and a magnetic field at the nucleus. Magnetic dipole interaction is beyond the present work. Here only the former two interactions will be discussed.

Isomer shift δ in a Mössbauer spectrum corresponds to the electric monopole interaction, and is related to the s-electron density through

$$\delta = C(\rho_A - \rho_S)({R_e}^2 - {R_g}^2) \qquad (2.13)$$

Where ρ_A, ρ_S denote the s-electron densities of nucleus in the absorber and emission source, respectively. C is a constant, R_e and R_g are the nuclear radius in its excited and ground state.

Quadrupole splitting ΔE_Q is related to the electric quadrupole interaction. It is proportional to the quadrupole moment eQ and the electric field gradient (EFG). EFG is given by a 3×3 tensor,

$$EFG = \vec{\nabla}\vec{E} = -\vec{\nabla}\vec{\nabla}V = \begin{vmatrix} V_{xx} & V_{xy} & V_{xz} \\ V_{yx} & V_{yy} & V_{yz} \\ V_{zx} & V_{zy} & V_{zz} \end{vmatrix} \qquad (2.14)$$

Where

$$V_{ij} = \frac{\partial^2 V}{\partial i \partial j} = q(3ij - r^2\delta_{ij})r^{-5}, (i, j = x, y, z)$$

In the principal axes system, because

1. Symmetric formal of the tensor $\rightarrow$ $V_{ij} = V_{ji}$,
2. Laplace equation requires EFG a traceless tenser $\rightarrow$ $\sum V_{ii} = 0$,
3. Off-diagonal elements vanish $\rightarrow$ $V_{ij} = 0$ ($i \neq j$)

Only two independent parameters are needed to describe the EFG, includes V_{zz} (in the selected system with $|V_{zz}| \geq |V_{xx}| \geq |V_{yy}|$), and asymmetry parameter $\eta = (V_{xx} - V_{yy})/V_{zz}$. For axial systems, $V_{xx} = V_{yy}$, therefore $\eta=0$. Then quadrupole interaction energy E_Q equal to

$$E_Q(I, m_I) = \frac{eQV_{zz}}{4I(2I-1)}\left[3m_I^2 - I(I+1)\right]\left(1 + \frac{\eta^2}{3}\right)^{\frac{1}{2}} \qquad (2.15)$$

Where I, m_I are nuclear spin state and magnetic spin numbers, respectively. And

$$\Delta E_Q = E_Q[I, m_I(1)) - E_Q[I, m_I(2)] \qquad (2.16)$$

In summary, the isomer shift δ and quadrupole splitting ΔE_Q obtained from Mössbauer spectrum are relative to information about electric density (mainly the sum of s-electrons) and electric field gradient around the Mössbauer atoms, in more detail, including oxidation state, spin state, bond properties, symmetry of electron distribution surrounding the Mössbauer atoms.

2.4 Impedance spectroscopy

Impedance is the measure of dependence of current to the applied voltage in a circuit. It can be denoted as

$$\mathrm{Z} = \frac{E(t)}{I(t)} \qquad (2.16)$$

Where $E(t)$ and $I(t)$ are the applied voltage and response current at time t, respectively. When an AC voltage is applied, the response will be also an AC current signal, i.e. for a periodic sinusoidal voltage, which is usually employed in the impedance spectroscopy,

$$\mathrm{E(t)} = \mathrm{E_0}\sin(\omega t) \qquad (2.17)$$

Where $\mathrm{E_0}$ is the amplitude of voltage, and ω is the radial frequency. The response current is

$$\mathrm{I(t)} = \mathrm{I_0}\sin(\omega t + \varphi) \qquad (2.18)$$

φ represents a phase shift of current signal from the applied voltage, I_0 is the maximum current. Obviously, I_0 and φ are independent to time t. Therefore, through lagging the circuit by a 1/4 period, we can obtain

$$\mathrm{E(t)} = \mathrm{E_0}\sin\left(\omega t - \frac{\pi}{2}\right) = \mathrm{E_0}\cos(\omega t) \qquad (2.19)$$

$$\mathrm{I(t)} = \mathrm{I_0}\sin\left(\omega t + \varphi - \frac{\pi}{2}\right) = \mathrm{I_0}\cos(\omega t + \varphi) \qquad (2.20)$$

Add equation (2.17) multiplied by j ($j^2 = -1$) to equation (2.19), and according to Euler's formula

$$\mathrm{e^{i\omega t}} = \cos(\omega t) + j\sin(\omega t)$$

We can obtain

$$\mathrm{E(t)} = \mathrm{E_0 e^{j\omega t}}$$

Similarly, by adding equation (2.18) multiplied by j with equation (2.20), we obtain

$$\mathrm{I(t)} = \mathrm{I_0 e^{j(\omega t+\varphi)}}$$

Therefore impedance

$$Z = \frac{E(t)}{I(t)} = \frac{E_0 e^{j\omega t}}{I_0 e^{j(\omega t+\varphi)}} = Z_0 e^{j\varphi} = Z_0 \cos(\varphi) + jZ_0 \sin(\varphi) = Re(Z) + Im(Z) \qquad (2.21)$$

Where impedance Z is denoted as a complex quantity with real part of Re(Z) and imaginary part of Im(Z).

There are three basic elements contributing to the total impedance, including

Resistor with resistance of R:

$$Z = R, \ \varphi = 0$$

Capacitor with capacitance of C:

$$Z = \frac{1}{j\omega C} = -\frac{j}{\omega C}, \qquad \varphi = \frac{\pi}{2}$$

Inductor with inductance of L:

$$Z = j\omega L, \qquad \varphi = -\frac{\pi}{2}$$

These three basic units are widely applied in the equivalent circuit constitution to model complex impedance signals. Mass transfer (diffusion) can create the Warburg impedance, which cannot be simply modeled with these three basic units. In the diffusion with "infinite" boundary, Warburg impedance

$$Z_w = \sigma\omega^{-1/2} - j\sigma\omega^{-1/2} \qquad (2.22)$$

Where σ is called Warburg coefficient, and relative to the diffusion coefficient of the diffusing species.

2.5 Electrochemistry in batteries

2.5.1 Battery assembly

A battery cell generally consists of three main parts: cathode, anode, and electrolyte. There're many kinds of battery cells used and developed, including

cylindrical cell, coin cell, prismatic cell, and pouch cell *et al*. Only the assembly of coin cell will be described below and employed in the thesis.

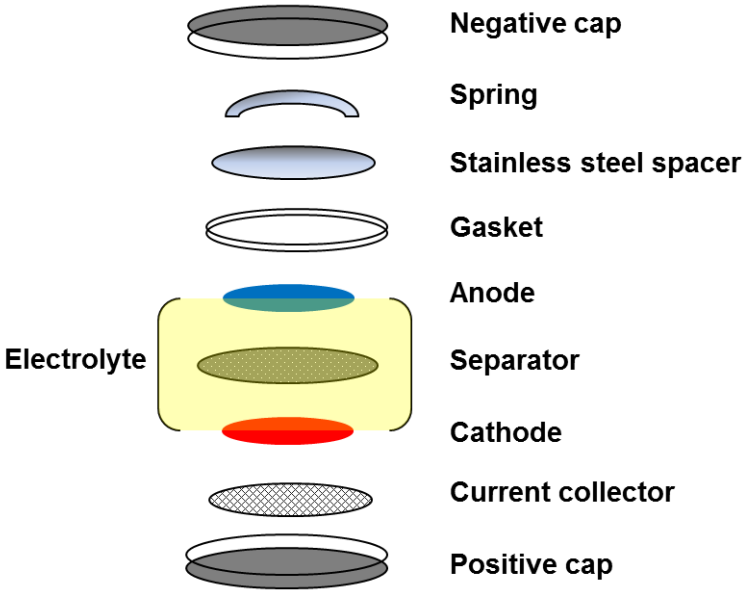

Figure 2.3 Schematic representation of the configuration of a coin cell

Fig. 2.3 shows the configuration of a general coin cell. An insulated separator with good Li^+/Na^+ ion diffusion property is inserted between the cathode and anode, to avoid the short-circuit situation. After assemble all the units in a cell, a vertical press is employed to compress the inner space and make the coin cell.

2.5.2 Electrochemical characterization

Cyclic Voltammetry (CV): In a CV measurement, potential cycles in a set range at a fixed rate, the response current is recorded with the potential. It is an efficient technic to identify properties of the redox reaction during battery cycling, i.e. the reaction reversibility, redox potential and reaction mechanism. Especially, in a reversible redox reaction, the peak current I_p on CV curve is given by the Randles-Sevcik equation (298 K)[9]

$$\mathrm{I}_p = (2.69 \times 10^5)\mathrm{n}^{\frac{3}{2}} A D^{\frac{1}{2}} C v^{\frac{1}{2}} \qquad (2.23)$$

where *n* is the number of electrons transferred in the redox reaction, *A* is the surface of electrode area, *D* the diffusion coefficient, *C* the concentration, and *v* the scan rate. Given a specific reversible reaction system, *n*, *A*, *D* and *C* are all constant, hence, the peak current I_p is proportional to $v^{1/2}$. Vice versa, a linear relationship between I_p and $v^{1/2}$ can confirm reversibility of the redox reaction in batteries.

Galvanostatic cycling: Galnanostatic cycling refers to that a cell is charged and discharged at a constant current in a set voltage range. It provides the charge and discharge properties for batteries, including the most important information for application — power density, redox voltage, cycle stability, rate capability *et al*.

2.6 Reference

(1) Giacovazzo, C.; Monaco, H. L.; Viterbo, D.; Scordari, F.; Gilli, G.; Catti, M. *Fundamentals of crystallography*; 5th ed.; Oxiford University, 2000.

(2) Rietveld, H. M. *J. Appl. Crystallogr.* **1969**, *2*, 65–71.

(3) McCusker, L. B.; Von Dreele, R. B.; Cox, D. E.; Louër, D.; Scardi, P. *J. Appl. Crystallogr.* **1999**, *32*, 36–50.

(4) Mössbaur, R. *Naturwissenschaften* **1958**, *45*, 538–539.

(5) Mössbaur, R. *Zeitschrift für Phys.* **1958**, *151*, 124–143.

(6) Mössbaur, R. *Science* **1962**, *1013*, 731–738.

(7) Mössbaur, R. *Hyperfine Interact.* **2000**, *126*, 1–12.

(8) Gütlich, P.; Bill, E.; Trautwein, A. X. *Mössbauer spectroscopy and Transition Metal Chemistry*; Springer, 2010.

(9) Randles, J. E. B. *Trans. Faraday Soc.* **1948**, *44*, 327–338.

3 Safety research of $Na_2FeP_2O_7$ as a Na-ion battery cathode

3.1 Introduction

Recently, $Li_2FeP_2O_7$ has been identified as a comparable cathode material for Li-ion batteries, with high redox voltage (3.5 V vs Li/Li^+), two-electron reaction possibility and low cost.[1] Inspired by the success of $Li_2FeP_2O_7$ as Li cathode material, our group and other researchers investigated $Na_2FeP_2O_7$ as a cathode material for sodium-ion batteries.[2,3] Based on Na-Fe-P-O system, it is a low-cost material with a moderate voltage (3V vs Na/Na^+) and excellent rate capability. However, to realize the practical application, $Na_2FeP_2O_7$ should be proven with a high safety without thermal/chemical decomposition during battery operation.

As cathode materials, the charged state is very oxidizing, and tends to decompose at high temperature and/or react with electrolyte. During this process, large amounts of heat and oxygen are released and finally lead to thermal runaway in batteries.[4] The thermal stabilities of $Li_2FeP_2O_7$ and its charged state ($LiFeP_2O_7$) have been surveyed by Tamaru et al.,[5] proving $Li_2FeP_2O_7$ even more stable than olivine $LiFePO_4$. In the charged state, a decomposition temperature of 1673 K for $LiFeP_2O_7$ is found much higher than that of 973 K for $FePO_4$. However, in the field of Na-ion batteries, the thermal stability of $Na_2FeP_2O_7$ (*P*-1) is still unclear, which cannot be directly estimated from the result of $Li_2FeP_2O_7$ ($P2_1/c$) due to the different crystallography. In this work, the charged state material ($NaFeP_2O_7$) was obtained with chemical oxidation of $Na_2FeP_2O_7$ and its thermal stability was investigated with *in-situ* high-temperature XRD and TG-DSC to evaluate the safety nature.

3.2 Research Methods

Material Synthesis: $Na_2FeP_2O_7$ was synthesized by conventional solid-state method. Stoichiometric amounts of $NaHCO_3$ (Wako, 99.5%), $FeC_2O_4 \cdot 2H_2O$ (Junsei, 99+%), and $(NH_4)_2HPO_4$ (Wako, 99%) were mixed together in acetone by planetary-type ball milling (400 rpm, 3h). Post vacuuming the acetone, the mixture was ground and pressed into cylindrical pellets by a hand press, then calcined at 873 K for 12 h in Ar/H2 (95:5) atmosphere. After cooling down to room temperature, pure $Na_2FeP_2O_7$ pellets were obtained and stored in glovebox as its unstable feature in air. The desodiated phase, $NaFeP_2O_7$ was synthesized by chemical oxidation method with NO_2BF_4 (Aldrich, 95+%) oxidizer in acetonitrile media as per the following equation:

$$Na_2Fe^{II}P_2O_7 + NO_2BF_4 \rightarrow NaFe^{III}P_2O_7 + NaBF_4 + NO_2 \uparrow \quad (333\ K)$$

The product was filtered out and dried at 333 K with vacuum.

Crystal structure characterization: Lab X-ray diffraction(XRD) and *In-situ* high temperature XRD was performed with a Rigaku RINT-TTR III powder diffractometer (operating at 50 kV, 300 mA) equipped with a Cu-Kα source (λ_1 = 1.5405 Å, λ_2 = 1.5443 Å). For high temperature measurement, the sample was heated (from RT ~ 873 K) inside a Rigaku Reactor-X chamber fitted with Beryllium window under steady N_2 flow. Diffraction patterns were acquired after keeping the sample at target temperatures for 1 h. Rietveld refinement was performed using TOPAS Version 3.0, and crystal structures were visualized by a computer program VESTA.[6]

Physical characterization: Mössbauer spectra were acquired with a Topologic System Inc. unit having a ^{57}Co γ-ray source duly calibrated with an α-Fe standard. Typically, ~0.1 g powder sample was sealed inside a Pb sample holder by polyethylene films and the spectra were collected for over 10 h in transmission mode and were

analyzed with MossWinn 3.0 software. Thermogravimetric (TG) and differential scanning calorimetry (DSC) study was conducted with a Rigaku ThermoPlus DSC 8230 unit from RT-873 K (heating rate = 5 K/min) under steady Ar flow (200 cc/min).

3.3 Results and discussion

3.3.1 Material synthesis

As-obtained $Na_2FeP_2O_7$ was characterized with Lab XRD. Its diffraction pattern and Rietveld refinement result are shown in Fig. 3.1. The Rietveld refinement result confirmed the sample purity. Only 2.6 wt% of $Na_4P_2O_7$ was detected as the impurity. Mössbauer spectrum is depicted in Fig.3.2, and the obtained relative parameters are listed in Table 3.1. The Mössbauer result proved 94.2% of Fe in the charge state of 2+, consistent to the high purity of $Na_2FeP_2O_7$.

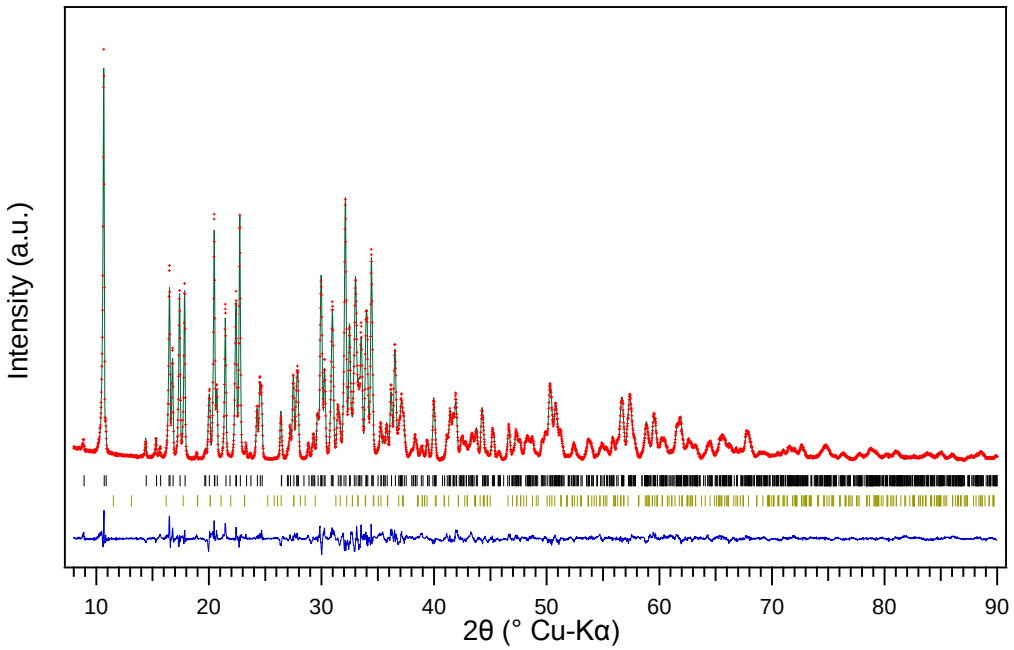

Figure 3.1 Lab XRD patterns of $Na_2FeP_2O_7$ sample. Experimental data points are shown as red crosses and the simulated powder pattern is shown as a green line. The difference profile and Bragg diffraction position (black vertical sticks) are shown below. The Brown sticks denote the diffraction position of $Na_4P_2O_4$ (2.6 wt%). R_{wp} = 6.794, GOF = 2.312.

Desodiated $NaFeP_2O_7$ was obtained by chemical oxidation of $Na_2FeP_2O_7$, the XRD pattern and Rietveld refinement results are drawn as Fig.3.4(c) at the convenience of whole understanding. The Mössbauer spectrum is shown in Fig. 3.2. The fitting result in Table 3.1 shows 98.4% of Fe^{3+}, confirming the successful oxidation.

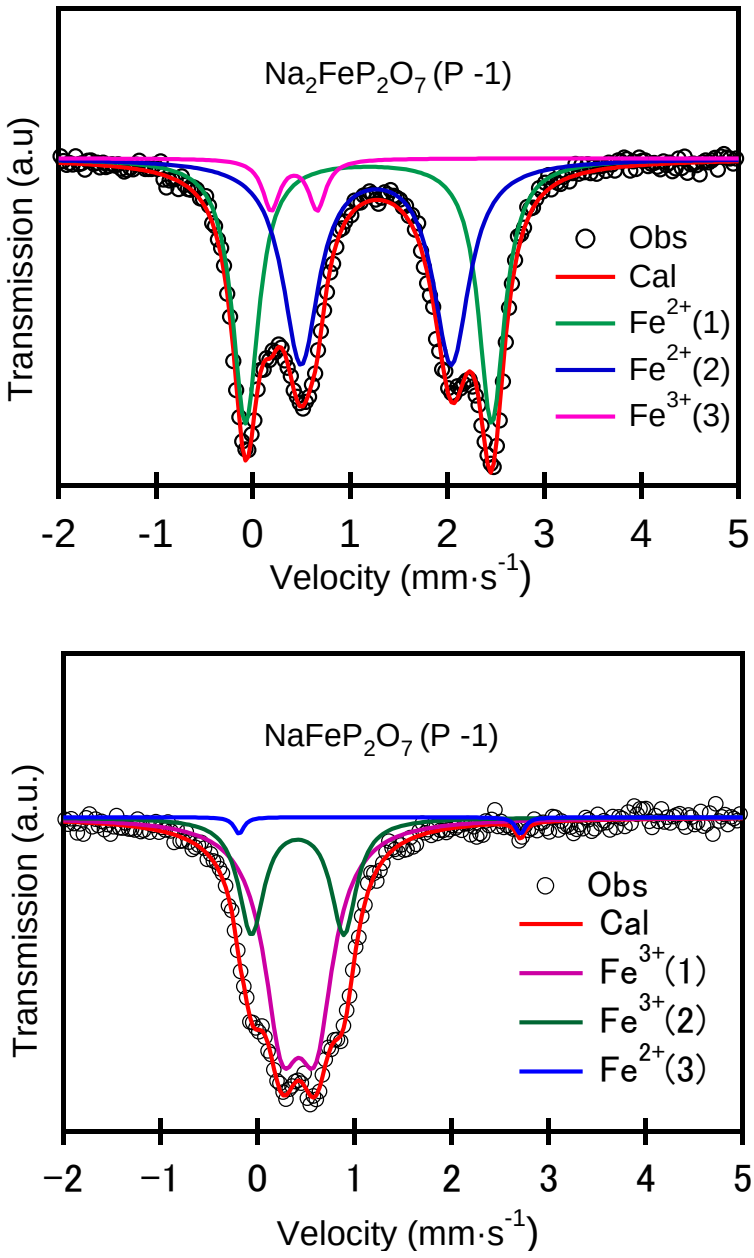

Figure 3.2 Mössbauer spectra of $Na_2FeP_2O_7$ and the desodiated $NaFeP_2O_7$.

Table 3.1 Relative refined parameters to the Mössbauer spectra of $Na_2FeP_2O_7$ and $NaFeP_2O_7$ samples.

	Fe species	Fraction	Isomer shift mm/s	Q. Splitting mm/s	Line width mm/s
$Na_2FeP_2O_7$ (*P*-1)	Fe^{2+} (1)	45.9%	1.191(1)	2.534(3)	0.325(4)
	Fe^{2+} (2)	48.3%	1.269(2)	1.549(5)	0.446(6)
	Fe^{3+} (3)	5.8%	0.425(6)	0.474(10)	0.216(11)
$NaFeP_2O_7$ (*P*-1)	Fe^{3+} (1)	69.3%	0.425(3)	0.345(13)	0.45(3)
	Fe^{3+} (2)	29.1%	0.414(4)	0.953(13)	0.31(2)
	Fe^{2+} (3)	1.6%	1.260(12)	2.90(2)	0.12(5)

3.3.2 Thermal properties of charged state upon phase transition

The charged (desodiated) cathode composition, in the presence of flammable organic solvents/ electrolyte, can trigger excessive heat generation, self-decomposition, loss of constituent oxygen and/or severe parasitic reactions at the electrode-electrolyte interfaces. These can create potential safety risk during battery operation. Hence, thermal study of charged cathodes is the key to know the operational safety of any potential cathode. After the structural evaluation, the thermal behavior of the charged β-$NaFeP_2O_7$ phase was examined.

Fig. 3.3 shows the TG-DSC profiles of β-$NaFeP_2O_7$ sample prepared by chemical oxidation of $Na_2FeP_2O_7$. The DSC curve depicts an exothermic peak with the onset point of 837 K with a moderate heat generation of 16 kJ/mol. The possibility of any chemical/thermal decomposition and/or related weight loss can be eliminated as the TG

curve shows no weight change. The combination of an exothermic peak with no weight change points at a possible phase transition of β-$NaFeP_2O_7$.

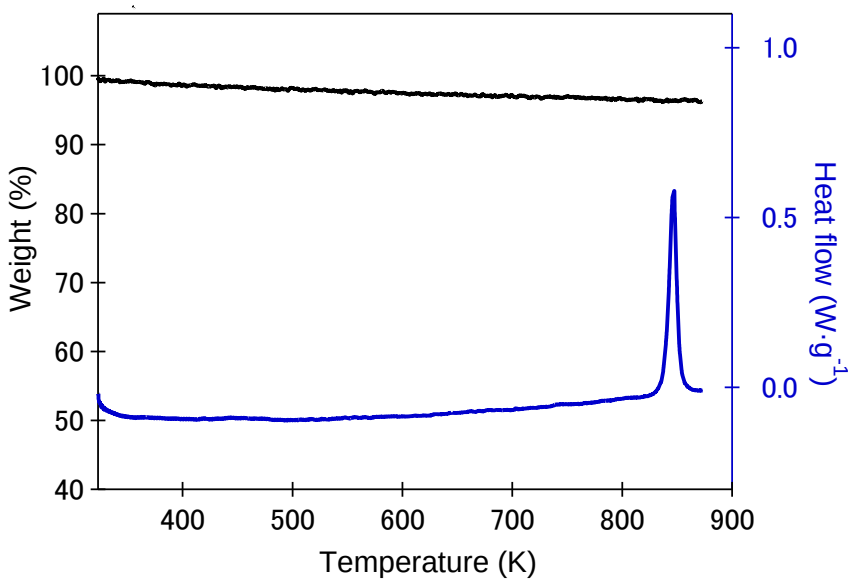

Figure 3.3 Thermal analysis (TG-DSC) curves of the desodiated state β-$NaFeP_2O_7$ under steady Ar flow. A sharp exothermic peak around 833~853 K is observed associated with no weight change, suggesting a possible phase-transition to a thermodynamically stable polymorph.

To verify this hypothesis, temperature-dependent XRD analysis on β-$NaFeP_2O_7$ sample was performed. As shown in Fig. 3.4(a), the characteristic diffraction pattern of initial β-$NaFeP_2O_7$ is retained intact up to 823 K. In sync with the DSC data, a transition is noticed in the narrow temperature window of 833~853 K, with new peaks emerging at the expense of old peaks. Upon the end of heating at 873 K, the starting β-$NaFeP_2O_7$ phase completely disappear to form α-$NaFeP_2O_7$. For reconfirmation, β-$NaFeP_2O_7$ sample is sintered at 873 K using the furnace. After cooling down, the as-obtained product is characterized with XRD (Fig. 3.4(b)), and is proven to be pure α-$NaFeP_2O_7$.

These results confirm the irreversible (triclinic P-1 → monoclinic $P2_1/c$ symmetry) phase transition of β-$NaFeP_2O_7$ cathode material.

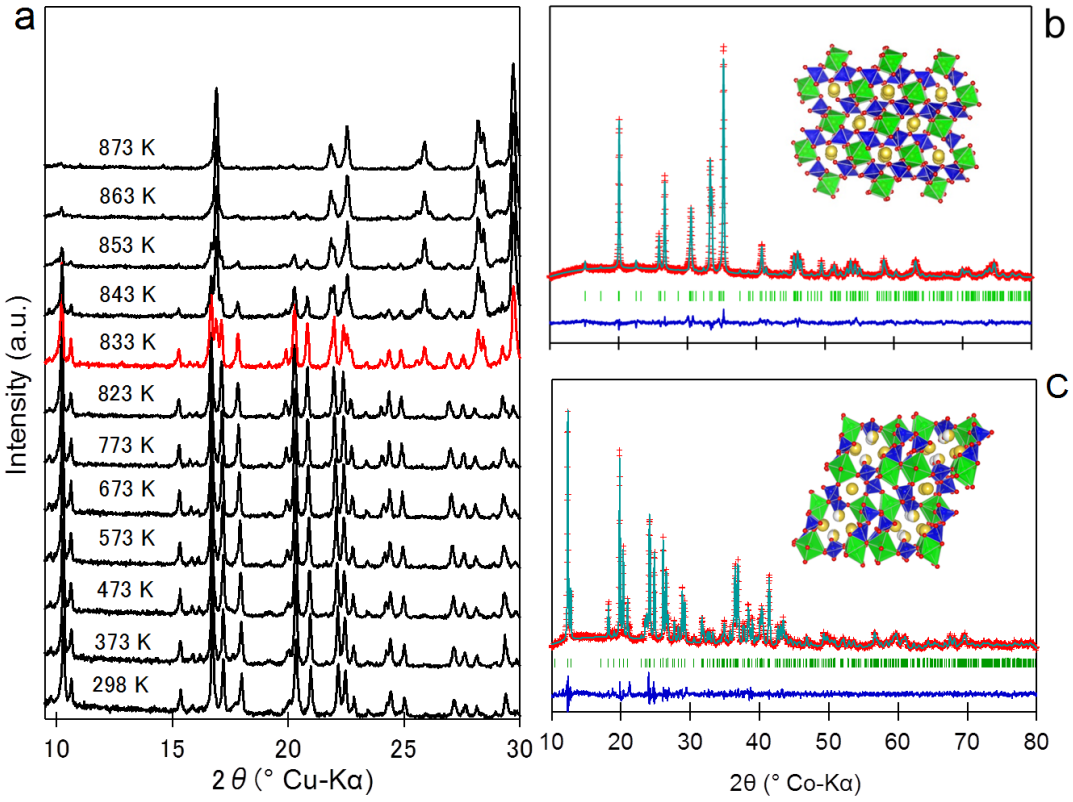

Figure 3.4 (a) *In-situ* high-temperature X-ray diffraction patterns of $NaFeP_2O_7$ showing the irreversible phase transition (833 K < T_t < 863 K) from *β*-$NaFeP_2O_7$ (triclinic, *P*-1) to α-$NaFeP_2O_7$ (monoclinic, $P2_1/c$). Rietveld refinement of (b) *β*-$NaFeP_2O_7$ and (c) α-$NaFeP_2O_7$ polymorphs are shown with the experimental data (red dots), simulated powder pattern (light blue line), Bragg diffraction positions (green ticks) and the difference between the experimental and theoretical patterns (blue line). The *inset* figures illustrates respective structural arrangement of the constituent FeO_6 octahedra (green), PO_4 tetrahedra (blue) and Na atoms (yellow).

3.3.3 Mechanism Discussion

Based on the above results, the β-$NaFeP_2O_7$ is metastable, as expected for a material prepared by soft desodiation. It can be rooted to two structural features as shown in Fig.3.5. First, in β-$NaFeP_2O_7$ phase, every alternate FeO_6 octahedra and PO_4 tetrahedra are connected by edge-sharing fashion. Owing to their dissimilar polyhedral size, the FeO_6 octahedra are highly distorted. Secondly, the coulombic Fe^{3+}–Fe^{3+} repulsion between neighboring FeO_6-FeO_6 is very strong due to their near proximity.[7] It makes the overall structure energetically unstable, which upon heating transforms to the stable α-$NaFeP_2O_7$ form having well separated symmetric FeO_6 octahedral units connected by PO_4 tetrahedra exclusively by corner-sharing mode. Similar temperature-induced phase transition has been recently noticed in the monoclinic $LiFeP_2O_7$ system,[5] which undergoes an irreversible polymorphic phase transition from $P2_1/c$ to $P2_1$ symmetry.

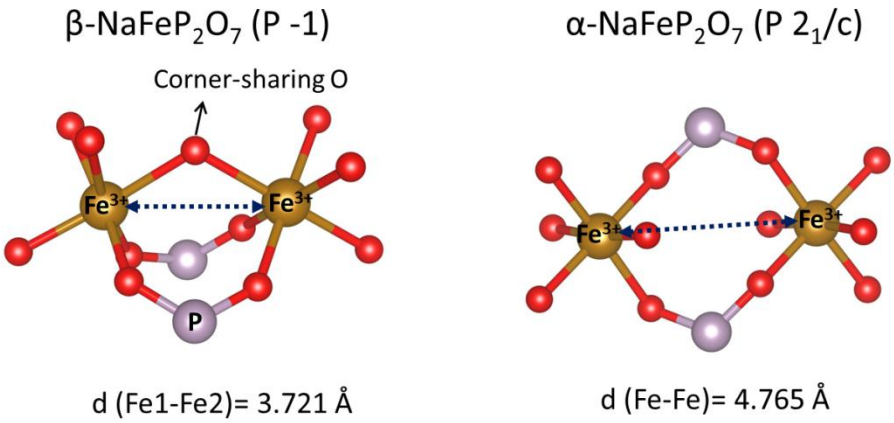

Figure 3.5 Schematic representation of electrochemical repulsion effect of Fe^{3+} ions in the α-$NaFeP_2O_7$ and β-$NaFeP_2O_7$ structures. Fe, P, and O are colored in brown, light purple and red, respectively.

The overall energetics of chemical/ electrochemical desodiation and β→α phase

transition in $Na_{2-x}FeP_2O_7$ system is shown in Fig. 3.6. While the desodiation process with $Fe^{2+} \rightarrow Fe^{3+}$ redox activity (at 2.98 V vs. Na/Na^+) involves large energy difference (2.98 eV) to form β-$NaFeP_2O_7$, it readily transforms to stable α-$NaFeP_2O_7$ polymorph with negligible 0.2 eV energy change. Attempts to intercalate sodium atoms into α-$NaFeP_2O_7$ were unsuccessful, making it electrochemically inactive, unlike isostructural $LiFeP_2O_7$ showing Li-insertion at 2.9 V.[8] The larger size of Na and surface energy may be the reason for such inactivity.

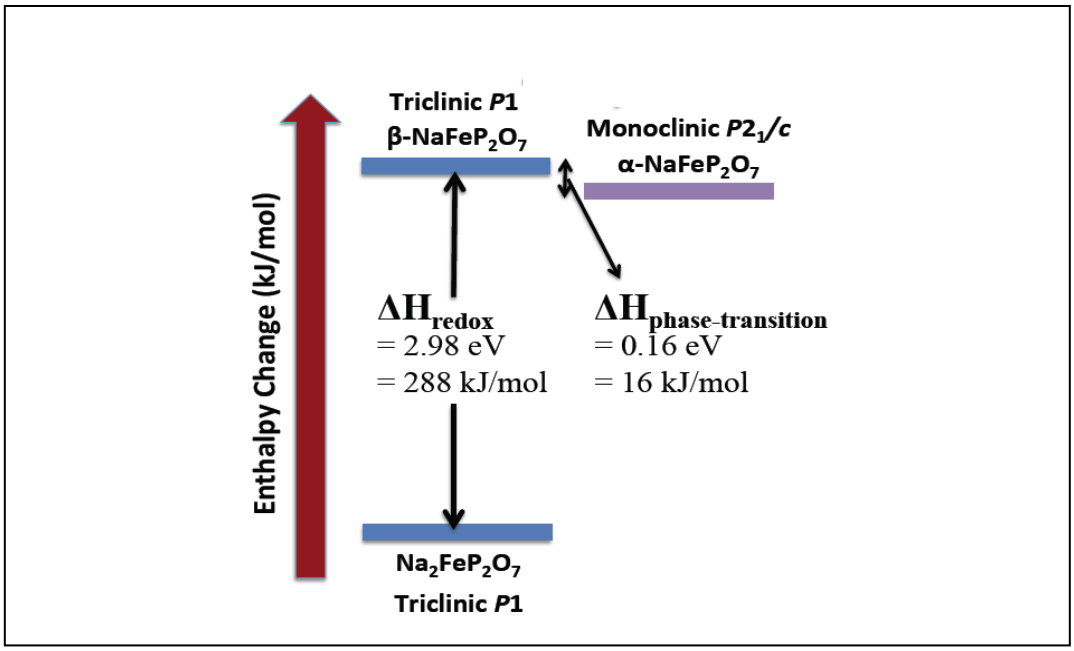

Figure 3.6 Enthalpy diagram of $Na_{2-x}FeP_2O_7$ polymorphs.

3.4 Conclusion

To summarize, pyrophosphate $Na_2FeP_2O_7$ has been shown to be a safe cathode material for sodium-ion batteries. Its charged state ($NaFeP_2O_7$) has high thermal stability up to 873 K, which does not involve any decomposition and/ or oxygen evolution, but undergoes polymorphic transition at 833 K from triclinic (*P*-1) to monoclinic ($P2_1/c$) phase. This thermal stability far exceeds to those of layered oxides

and at least comparable to other polyanionic cathodes such as olivine ($NaFePO_4$). The higher stability can be rooted to the inherent high stability of pyrophosphate $(P_2O_7)^{4-}$ building blocks. Thus, pyrophosphate cathodes tend to deliver higher operational safety.

3.5 Reference

(1) Nishimura, S.; Nakamura, M.; Natsui, R.; Yamada, A. *J. Am. Chem. Soc.* **2010**, *132*, 13596–13597.

(2) Kim, H.; Shakoor, R. A.; Park, C.; Lim, S. Y.; Kim, J.-S.; Jo, Y. N.; Cho, W.; Miyasaka, K.; Kahraman, R.; Jung, Y.; Choi, J. W. *Adv. Funct. Mater.* **2013**, *23*, 1147–1155.

(3) Barpanda, P.; Ye, T.; Nishimura, S.; Chung, S.-C.; Yamada, Y.; Okubo, M.; Zhou, H.; Yamada, A. *Electrochem. commun.* **2012**, *24*, 116–119.

(4) Balakrishnan, P. G.; Ramesh, R.; Prem Kumar, T. *J. Power Sources* **2006**, *155*, 401–414.

(5) Tamaru, M.; Chung, S. C.; Shimizu, D.; Nishimura, S.; Yamada, A. *Chem. Mater.* **2013**, *25*, 2538–2543.

(6) Momma, K.; Izumi, F. *J. Appl. Crystallogr.* **2011**, *44*, 1272–1276.

(7) Chung, S. C.; Barpanda, P.; Nishimura, S.-I.; Yamada, Y.; Yamada, A. *Phys. Chem. Chem. Phys.* **2012**, 8678–8682.

(8) Padhi, A. K.; Nanjundaswamy, K. S.; Masquelier, C.; Okada, S.; Goodenough, J. B. *J. Electrochem. Soc.* **1997**, *144*, 1609–1613.

4 Ionic conduction mechanism researches in $Na_{2-x}M_{1+x/2}P_2O_7$-type structure using $Na_{2-x}Mg_{1+x/2}P_2O_7$ as a model

4.1 Introduction

Although lithium ion battery technology is still prominent as a high-energy density power source, future application of secondary batteries will be much extended thereby utilizing abundant elements becomes important. Sodium ion battery technology has attained renewed interest[1,2,3] especially for larger scale applications, due to the natural abundance and low cost of Na[4,5]. Searching for a new earth-abundant cathode materials, Yamada group[6,7] and other researchers[8,9] have recently identified $Na_{2-x}Fe_{1+x/2}P_2O_7$ as a promising candidate with moderate redox potential at 3 V versus Na/Na^+, reasonable reversible capacity about 100 mAh/g, and a good rate capability with 85 % of its initial capacity retained even under a high rate of 5C.[6]

As the high-rate capability requires superior transport properties, high ionic conductivity in the $Na_{2-x}M_{1+x/2}P_2O_7$-type compounds is anticipated in general. Therefore, understanding of their ionic conduction mechanism in the atomic scale is of interest based on the precise crystal structure. Redox activity can introduce undesirable structural imperfections into $Na_{2-x}M_{1+x/2}P_2O_7$ (M = transition metal), i.e. sodium nonstoichiometry and hole defect at the transition metal sites. Therefore, the redox-inactive Mg variant, $Na_{2-x}Mg_{1+x/2}P_2O_7$, is chosen as a model system in order to minimize these contributions to Na ion transport. Additionally, $Na_{2-x}Mg_{1+x/2}P_2O_7$ might be a good ionic conductor and potentially a solid electrolyte.

In the 1970s, $Na_{2-x}Mg_{1+x/2}P_2O_7$ was initially designated as $Na_7Mg_{4.5}(P_2O_7)_4$ by Hanic et al.,[10,11] and its ionic conductivity was investigated by Znášik et al.[12] More

recently, Erragh et al. reinvestigated the chemical composition, and concluded $Na_{3.64}Mg_{2.18}(P_2O_7)_2$ ($Na_{1.82}Mg_{1.09}P_2O_7$) is the composition in the pure phase[13]. Most of the previous reports found deviations from the ideal stoichiometric $Na_2MP_2O_7$, and significant positional disorder at one Na site was observed. This kind of disordering is frequently found in good ionic conductors, as extended and shallow site potentials induce large thermal vibrations.

However, to the best of our knowledge, only glassy $Na_{1.82}Mg_{1.09}P_2O_7$ has been studied[14] before. The conductivity of pure crystalline sample has never been obtained. In the present work, we succeeded to synthesize a pure polycrystalline $Na_{1.82}Mg_{1.09}P_2O_7$ sample. The crystal structure and ionic conductivity at temperatures up to 773 K were investigated using synchrotron X-ray diffraction and AC impedance spectroscopy, followed by general discussions on Na ionic diffusion mechanism in this type of structure.

4.2 Research methods

Material synthesis: Two kinds of solid-state methods have been employed for $Na_{1.82}Mg_{1.09}P_2O_7$ synthesis: two-step method and direct method.

In the two-step method, $Na_4P_2O_7$ and $Mg_2P_2O_7$ have been synthesized at first, using the stoichiometric amounts of NaH_2PO_4 (Wako, 99%) and $NaHCO_3$ (Wako, 99%) as precursors for $Na_4P_2O_7$, and $Mg(OH)_2$ (Wako, 99.9%) together with $(NH_4)_2HPO_4$ (Wako, 99%) for $Mg_2P_2O_7$. The precursors were mixed by planetary-type ball milling (400 rpm, 7h), pressed into cylindrical pellets by a hand press, and sintered in Ar atmosphere at high temperatures (873 K for $Na_4P_2O_7$ synthesis, and 1173 K for the case of $Mg_2P_2O_7$). Then,

stoichiometric mixture of $Na_4P_2O_7$ and $Mg_2P_2O_7$ were prepared with ball milling, and also pressed into cylindrical pellets for $Na_{1.82}Mg_{1.09}P_2O_7$ synthesis at 973 K in Ar atmosphere.

In the direct synthesis method, stoichiometric amounts of NaH_2PO_4 (Wako, 99%), $Mg(OH)_2$ (Wako, 99.9%), and $(NH_4)_2HPO_4$ (Wako, 99%) were mixed by planetary-type ball milling. The mixture was then pressed into cylindrical pellets, and calcined at 973 K for 12 h in Ar atmosphere to obtain the pure product.

Thermal analysis: TG-DTA was conducted with a SII EXSTAR 6000 unit from RT up to 1273 K (heating rate = 20 K/min), alumina pans have used as the containers and measurement was operated in Ar atmosphere (flow velocity = 200 ml/min).

Laboratory X-ray diffraction: Powder X-ray diffraction was performed with a Bruker AXS D8 ADVANCE powder diffractometer using Co-Kα radiation (λ_1 = 1.78897 Å).

Synchrotron powder X-ray diffraction: Synchrotron XRD was carried out at various temperatures ranging from room temperature to 773 K, on a multiple-detector system[15,16,17] at BL4B2 station of Photon Factory, High Energy Accelerator Research Organization (KEK), Japan. The monochromatized X-ray wavelength was calibrated to be 1.196188 Å by measurement of SRM640c. The 2θ step interval and range were 0.005° and 5-154° respectively. Rietveld refinement was performed using TOPAS Version 3.0 or TOPAS-Academic Version 5 program, and the crystal structure and volumetric data were visualized by a computer program VESTA[18].

Impedance measurement: A powder sample was pressed into a cylindrical disk under 10 MPa, and then sintered at 973 K to maximize the density. Sizes of the sintered disks were typically 10 mm in diameter, 2 mm thick. The measured density is 2.25 g/cm^3, which corresponds to 79.2% of the theoretical value (2.84 g/cm^3). After that, both sides of the

disk were coated with Au film (500 nm in thickness) by a DC sputtering coater, and re-annealed at 773 K in Ar atmosphere.

The AC impedance measurements were operated with a SI 1260 solartron impedance/gain-phase analyzer coupled to a 1296 dielectric interface. The scanning frequency range is 1 MHz~0.01 Hz, and an applied AC voltage of 100 mV was used. The cylindrical disk was measured during heating from RT up to 773 K in dry-air atmosphere. The step interval is set to 50 K, and the sample disk was held to equilibrate at the each temperature for 1h before measurements started.

4.3 Results and discussion

4.3.1 Material preparation

Previously, literatures[11–13]reported that $Na_{1.82}Mg_{1.09}P_2O_7$ had been obtained using $Na_4P_2O_7$ and $Mg_2P_2O_7$. Thus, this method was firstly tried in the present work, and the related reaction equations can be written as follows.

$$2NaH_2PO_4 + 2NaHCO_3 \rightarrow Na_4P_2O_7 + 3H_2O\uparrow + 2CO_2\uparrow \text{ (873 K)}$$

$$2Mg(OH)_2 + 2(NH_4)_2HPO_4 \rightarrow Mg_2P_2O_7 + 5H_2O\uparrow + 4NH_3\uparrow \text{ (1173 K)}$$

$$0.91Na_4P_2O_7 + 1.09Mg_2P_2O_7 \rightarrow 2Na_{1.82}Mg_{1.09}P_2O_7 \text{ (973 K)}$$

Fig. 4.1 shows the procedure of two-step synthesis, phase pure $Na_4P_2O_7$ and $Mg_2P_2O_7$ were obtained respectively, and then used for $Na_{1.82}Mg_{1.09}P_2O_7$ synthesis. The XRD pattern of as-obtained $Na_{1.82}Mg_{1.09}P_2O_7$ is depicted as the top curve in Fig. 4.1, and its Rietveld refinement result is shown as Fig. 4.2. The relatively low *R* values indicated the high purity of product.

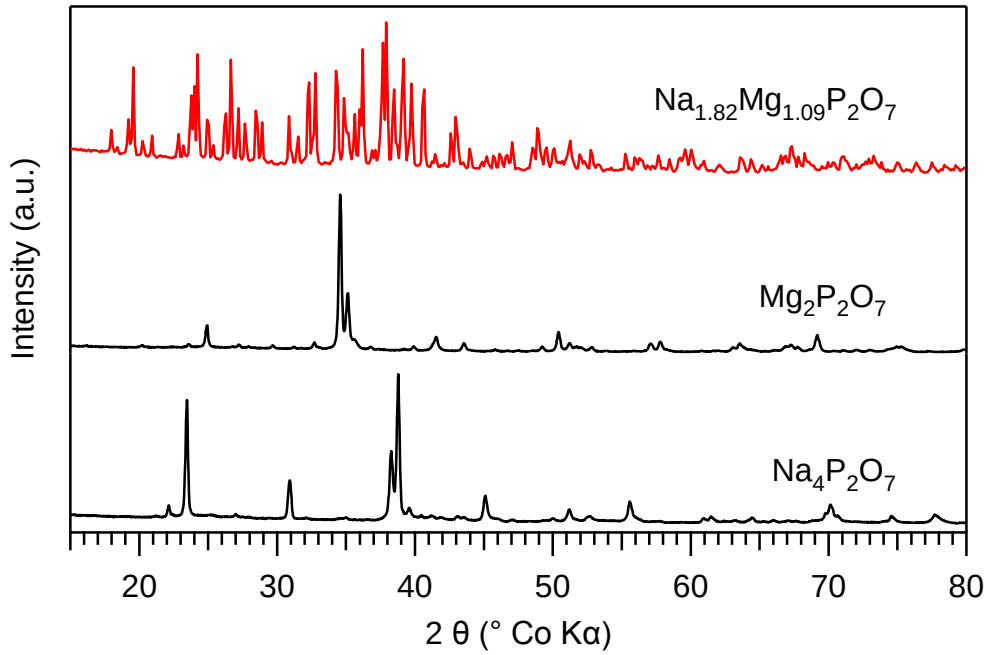

Figure 4.1 XRD patterns of intermediates in the two-step method

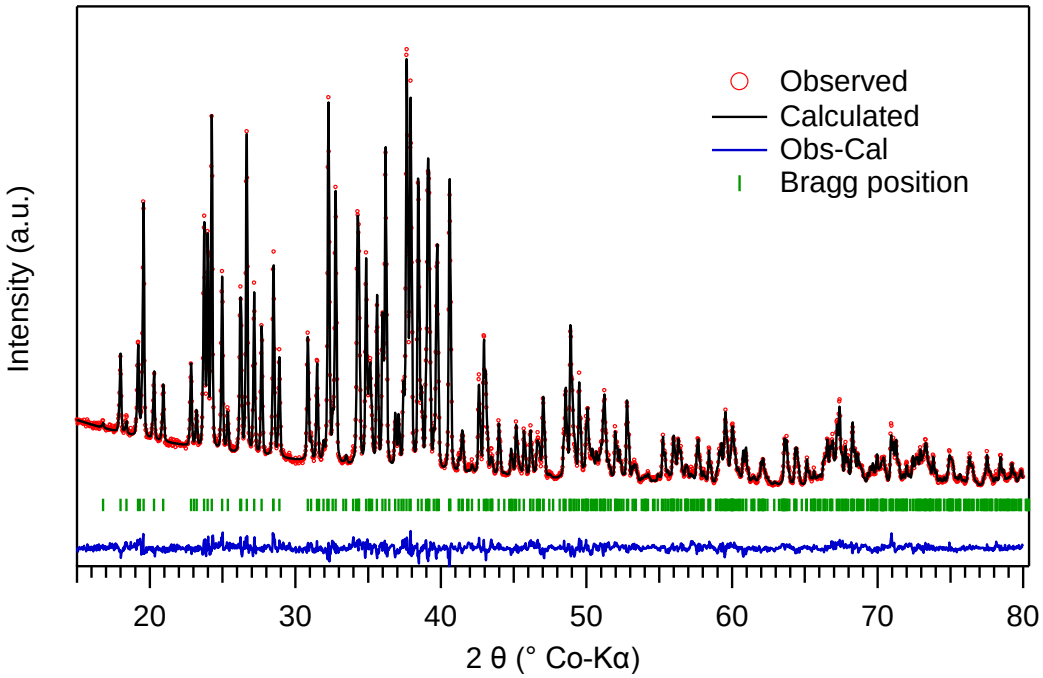

Figure 4.2 Rietveld refinement result for $Na_{1.82}Mg_{1.09}P_2O_7$ obtained with two-step method. (R_{wp} = 4.621, GOF = 1.839)

Although above results prove that pure $Na_{1.82}Mg_{1.09}P_2O_7$ can be obtained with two-step method, always the final product was found in gray color. That indicates some amounts of carbon formed from the decomposition of carbonate ($NaHCO_3$) precursor. Because conductivity is significantly sensitive to doping elements, even a trace of carbon should be removed. To absolutely remove carbon and simplify the synthesis, a direct synthesis method was proposed, which reaction can be denoted as the followed equation.

$$1.82NaH_2PO_4 + 1.09Mg(OH)_2 + 0.18(NH_4)_2HPO_4$$

$$\rightarrow Na_{1.82}Mg_{1.09}P_2O_7 + 3.18H_2O\uparrow + 0.36NH_3\uparrow \ (973\ K)$$

Pure white powders were obtained by this direct-synthesis method. The XRD pattern and Rietveld refinement result are depicted as Fig. 4.3. Compared to that obtained from two-step method, $Na_{1.82}Mg_{1.09}P_2O_7$ obtained by direct synthesis shows better Goodness of fitting (GOF) value.

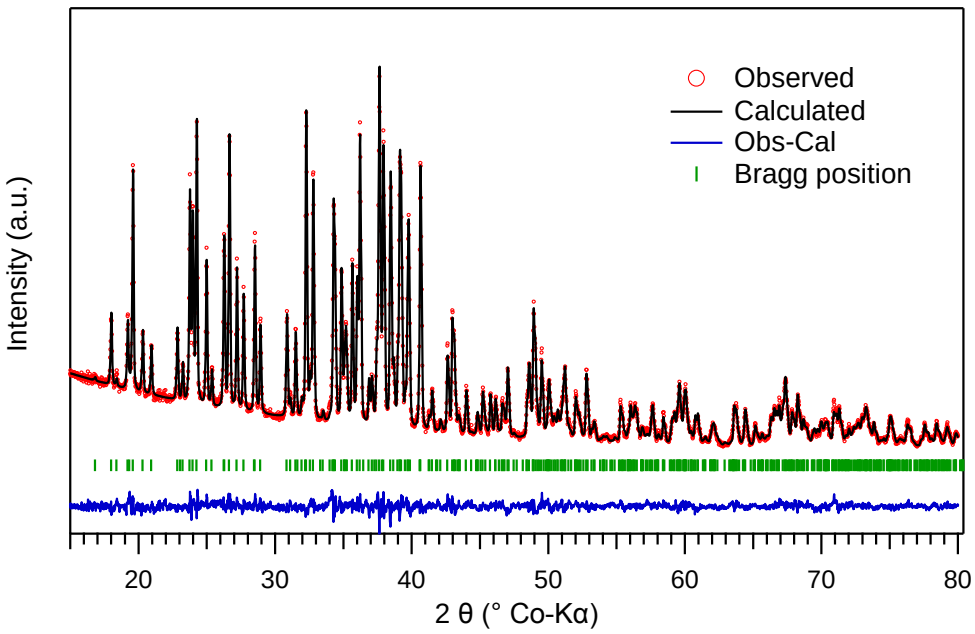

Figure 4.3 Rietveld refinement results for $Na_{1.82}Mg_{1.09}P_2O_7$ obtained with direct synthesis method. (R_{wp} = 4.621, GOF = 1.607)

4.3.2 Crystal Structure characterizations

Synchrotron XRD has been conducted on the direct-synthesis product. The S-XRD data were employed to characterize the crystal structure of $Na_{1.82}Mg_{1.09}P_2O_7$. Fig. 4.4 depicts the S-XRD patterns measured from 300 K up to 773 K and their Rietveld refinement results.

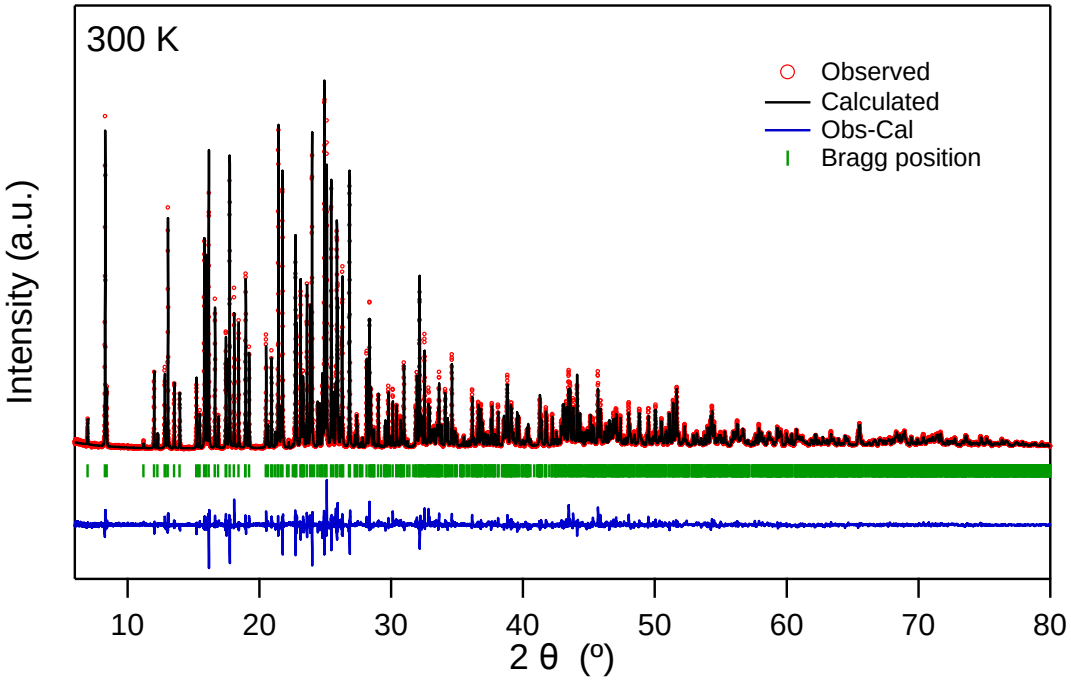

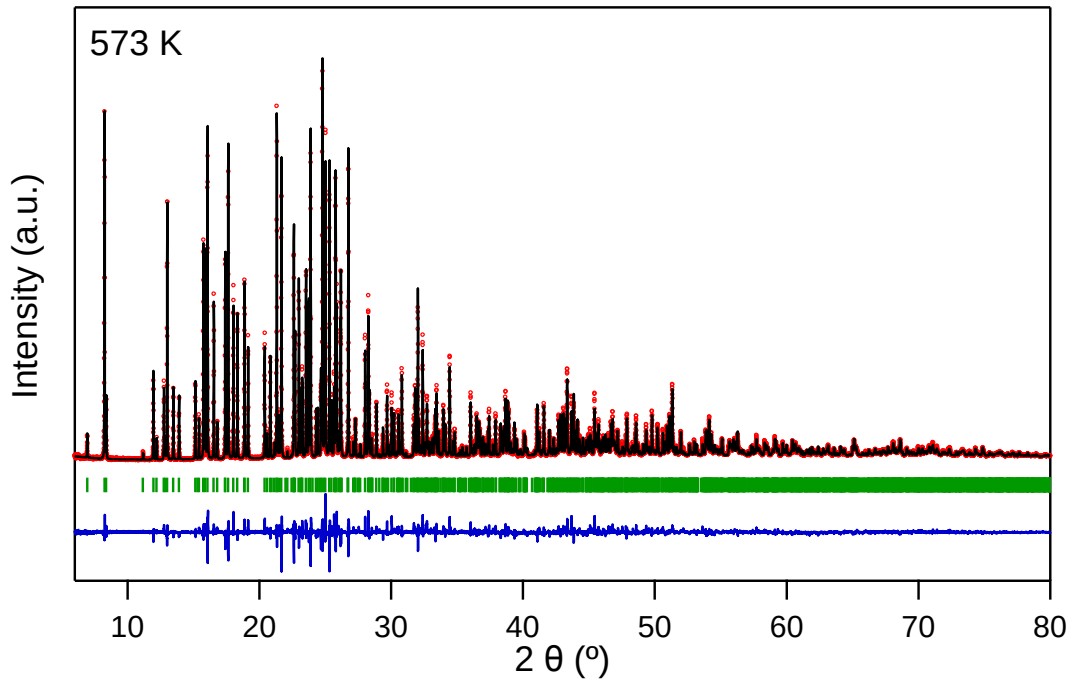
573 K
Intensity (a.u.)
10
20
30
40
50
60
70
80
2 θ (º)

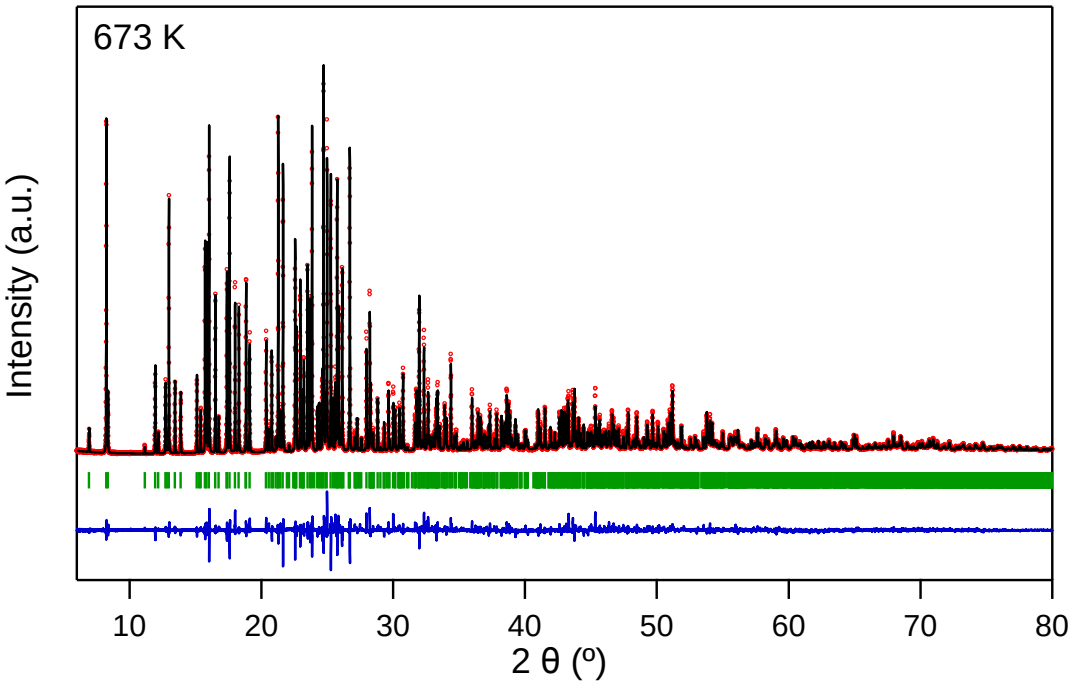
673 K
Intensity (a.u.)
10
20
30
40
50
60
70
80
2 θ (º)

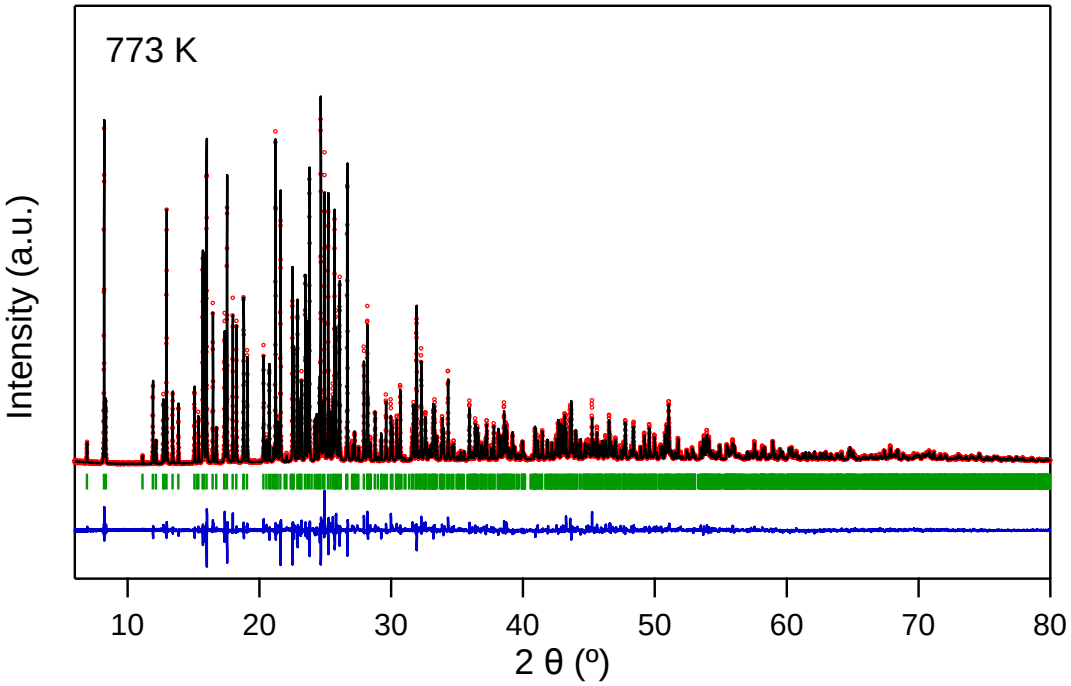

Figure 4.4 Rietveld refinement of $Na_{1.82}Mg_{1.09}P_2O_7$ to S-XRD data collected at 300 K (R_p= 7.35%, R_{wp}= 8.52%, χ^2= 3.12); 573 K (R_p=6.70%, R_{wp}=7.91%,χ^2=3.55); 673 K (R_p=6.73%, R_{wp}=8.21%, χ^2=2.99); and 773 K (R_p=6.57%, R_{wp}=7.76%, χ^2=3.58)

Table 4.1 The lattice parameters of $Na_{1.82}Mg_{1.09}P_2O_7$ at various temperatures. The last row lists literature-reported data after standardization according to definite rules[19]

Temperature (℃)	*a* (Å)	*b* (Å)	*c* (Å)	*α* (°)	*β* (°)	*γ* (°)	Vol (Å^3)
27	6.39258(3)	9.41968(4)	10.90912(4)	64.6804(2)	80.2968(2)	73.5798(2)	568.720(4)
300	6.41845(2)	9.47593 (3)	10.95125(4)	64.6881(2)	80.3956(2)	73.5067(2)	576.548(3)
400	6.42881(2)	9.49758(3)	10.96812(3)	64.6926(2)	80.4314(2)	73.4797(2)	579.657(3)
500	6.43873(2)	9.51873(3)	10.98396(3)	64.6996(2)	80.4692(2)	73.4519(2)	582.663(3)
Room Temp.[13]	6.38200	9.40890	10.90100	64.7740	80.3600	73.6030	567.233

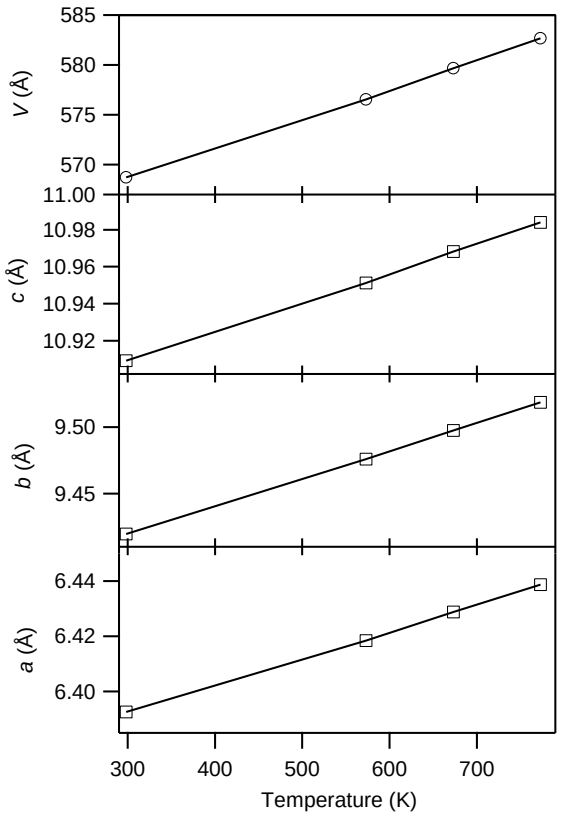

Figure 4.5 The linear relationship of lattice parameters (*a*, *b*, *c* and volume) to temperature in $Na_{1.82}Mg_{1.09}P_2O_7$.

The structure model of Erragh *et al.*[13] has been used as a starting model, which used a triclinic symmetry (*P* -1). The lattice parameters obtained from these four XRD patterns are listed in Table 4.1, compared with those of the starting model. There is no anomalous difference among the four S-XRD patterns, except for continuous shifts of the peaks to lower angles as the thermal expansion of the unit cell. Fig. 4.5 depicts the linear relationship of lattice parameters to temperature, proving that $Na_{1.82}Mg_{1.09}P_2O_7$ is thermally stable up to 773 K. This stability can also be confirmed by the TG-DTA result in Fig. 4.6. Except for one endothermic peak at 1083 K indicating the melting of $Na_{1.82}Mg_{1.09}P_2O_7$, there is no other obvious DTA peak before 1100 K, confirming the

thermal stability of $Na_{1.82}Mg_{1.09}P_2O_7$. Therefore, atomic coordination in $Na_{1.82}Mg_{1.09}P_2O_7$ must be identical in the temperature range of 300 K~773 K. Based on this reason, only the crystal structure at 300 K is elucidated in the present work as an example.

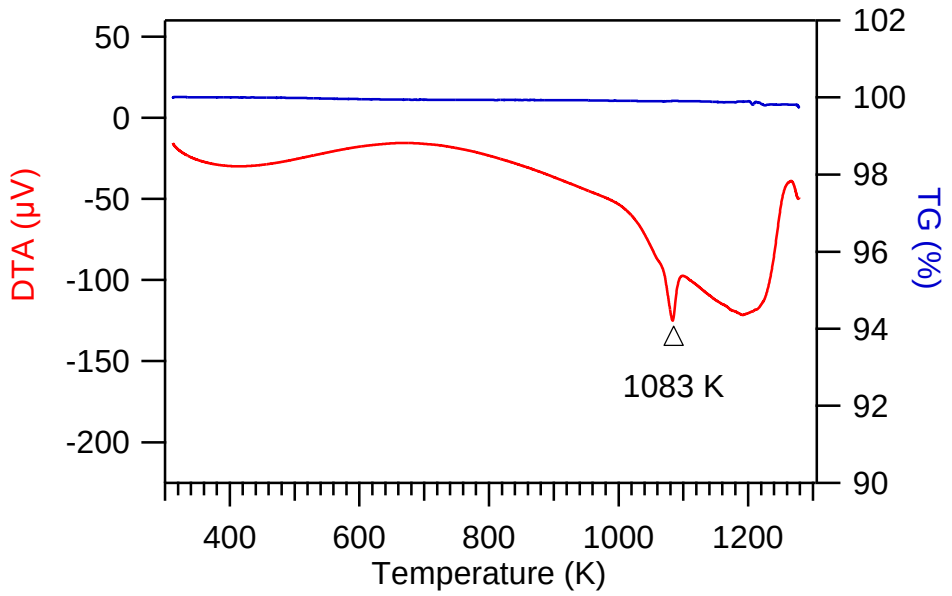

Figure 4.6 TG-DTA result of $Na_{1.82}Mg_{1.09}P_2O_7$ measured in Ar atmosphere. The endothermic peak at 1083 K indicates the melting of $Na_{1.82}Mg_{1.09}P_2O_7$, slightly lower than the reported melting point (1105 K).[10]

During the Rietveld refinement from Erragh *et al*'s model, since Na^+ and Mg^{2+} have almost the same atomic scattering factor due to their identical electron number, X-ray diffraction is inadequate to deduce the accurate ratio of Na^+ and Mg^{2+}. Therefore, the total composition ratio of Na^+ and Mg^{2+} was fixed to the initial number (1.82 : 1.09). There are 4 crystallographic Na sites in the initial model: Na(1) with partial substitution of Mg (Mg_{Na}^{+}), Na(2) and Na(3) with full occupancies, and a positional disorder site Na(4).

To reproduce the positional disorder in the crystal structure, a site splitting model was employed. The number of sub-site used affects the final Rietveld refinement result significantly (Fig. 4.7). Although *Erragh et al*'s structure employed 3 sub-sites model, Fig. 4.7 shows that 4 sub-sites model leads to a much lower *R* value, therefore is more effective to reproduce the Na disorder. Consequently, 4 sub-sites (denoted as Na(4)/Na(5)/Na(6)/Na(7)) were introduced in the origin Na(4) site for Rietveld refinement. Initial refinement shown that occupancies of the 4 sub-sites are similar therefore an equal value of 0.205 at each site were used in the subsequent refinement. In addition, the positional restriction of Na and Mg at Na(1) site was removed for a decreased *R* value. The final refinement XRD patterns are depicted in Fig. 4.4, and the detailed structure information is listed in Table 4.2.

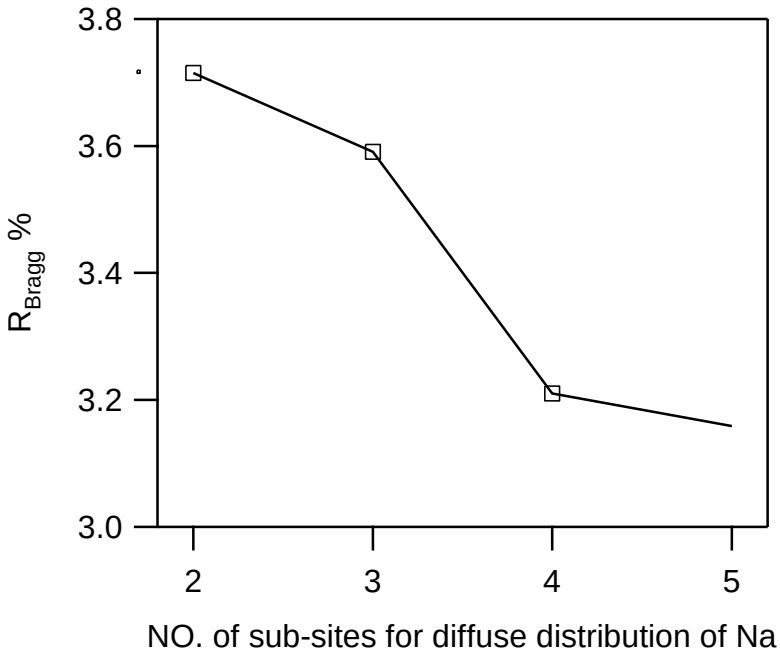

Figure 4.7 Relationship of R_{Bragg} and number of sub-sites employed for description of Na disorder.

Table 4.2 Atomic positions, occupancies, and isotropic atomic displacement parameters of $Na_{1.82}Mg_{1.09}P_2O_7$ obtained through Rietveld refinement against S-XRD pattern (300 K).

site type	site label	multiplicity	*x*	*y*	*z*	occupancy	B ($Å^2$)
Mg	Mg1	2	0.2288(3)	0.1093(2)	0.28451(19)	1	0.79(4)
Mg	Mg2	2	0.1441(3)	0.7622(3)	0.23781(19)	1	0.57(4)
Na	Na1	2	0.5374(7)	0.2934(5)	0.0255(4)	0.82	1.04(7)
Mg	MgNa	2	0.502(3)	0.268(2)	0.0238(18)	0.18	1.04(7)
Na	Na2	2	0.0760(4)	0.5153(3)	0.8387(3)	1	2.90(7)
Na	Na3	2	0.2778(5)	0.0376(3)	0.6144(3)	1	4.49(8)
Na	Na4	2	0.0479(17)	0.4831(20)	0.5079(18)	0.205	1.12(12)
Na	Na5	2	0.1623(18)	0.4404(18)	0.5271(15)	0.205	1.12(12)
Na	Na6	2	0.2591(18)	0.4401(17)	0.5408(14)	0.205	1.12(12)
Na	Na7	2	0.3641(18)	0.4297(15)	0.5582(12)	0.205	1.12(12)
P	P1	2	0.0772(3)	0.1582(2)	0.04676(16)	1	1.24(4)
P	P2	2	0.3784(3)	0.14031(20)	0.81600(17)	1	0.97(4)
P	P3	2	0.4301 (3)	0.3941(2)	0.28255(18)	1	1.25(4)
P	P4	2	0.7937(3)	0.2285(2)	0.46279(17)	1	1.14(4)
O	O1	2	0.5190(6)	0.0171(4)	0.2018(4)	1	1.45(9)
O	O2	2	0.4614(6)	0.7651(4)	0.1915(4)	1	1.54(9)
O	O3	2	0.1882 (6)	0.2455(5)	0.7252(4)	1	0.86(8)
O	O4	2	0.2751(6)	0.0755(4)	0.9705(4)	1	0.88(9)
O	O5	2	0.1185(5)	0.7761(4)	0.0409(3)	1	0.64(9)

O	O6	2	0.0542(6)	0.0208(5)	0.1846(4)	1	0.85(8)
O	O7	2	0.1464(6)	0.2876(4)	0.0681(4)	1	1.27(9)
O	O8	2	0.7172(6)	0.0736(4)	0.5384(4)	1	1.29(9)
O	O9	2	0.0543(6)	0.7699(5)	0.6621(4)	1	1.53(9)
O	O10	2	0.1224(6)	0.7216(4)	0.4439(4)	1	1.14(8)
O	O11	2	0.5817(6)	0.3761(4)	0.3989(3)	1	1.11(9)
O	O12	2	0.2185(6)	0.5139(4)	0.2990(4)	1	0.99(9)
O	O13	2	0.3964(6)	0.2280(4)	0.3246(4)	1	1.62(10)
O	O14	2	0.5551(7)	0.4522(5)	0.1470(4)	1	2.91(11)

Table 4.3 Selected bond lengths and bond valence sum value in $Na_{1.82}Mg_{1.09}P_2O_7$

P(1)-P(4)= 1.595(7)	P(2)-O(1)= 1.523(6)	P(3)-O(11)= 1.648(6)	P(4)-O(8)= 1.513(7)
P(1)-P(5)= 1.524(6)	P(2)-O(2)= 1.509(6)	P(3)-O(12)= 1.537(7)	P(4)-O(9)= 1.532(7)
P(1)-P(6)= 1.525(7)	P(2)-O(3)= 1.525(7)	P(3)-O(13)= 1.500(7)	P(4)-O(10)= 1.510(7)
P(1)-P(7)= 1.522(7)	P(2)-O(4)= 1.619(6)	P(3)-O(14)= 1.510(7)	P(4)-O(11)= 1.637(7)
<P(1)-O>= 1.5413	**<P(2)-O>= 1.5439**	**<P(3)-O>= 1.5488**	**<P(4)-O>= 1.5477**
BVS= 4.924	**BVS= 4.906**	**BVS= 4.867**	**BVS= 4.870**

Mg(1)-O(6)= 2.201(7)	Mg(2)-O(2)= 2.011(6)
Mg(1)-O(7)= 2.280(7)	Mg(2)-O(3)= 2.110(5)
Mg(1)-O(8)= 1.965 (7)	Mg(2)-O(5)= 2.128(7)
Mg(1)-O(9)= 1.989(7)	Mg(2)-O(6)= 2.171(7)
Mg(1)-O(13)= 1.960(7)	Mg(2)-O(10)= 2.100(6)

Mg(1)-O(1)= 2.051(7)	Mg(2)-O(12)= 2.071(6)
<M(1)-O>= 2.0744	**<M(2)-O>= 2.0983**
BVS= 2.253	**BVS= 2.025**

Some selected bond lengths and bond valence sum values for Mg and P are listed in Table 4.3, which are consistent with the previous report[13]. This information proves that the obtained crystal structure is reasonable, and adequate for the following discussion.

The crystal structure of $Na_{1.82}Mg_{1.09}P_2O_7$ is described as Fig. 4.8. There're two crystallographic MgO_6 octahedra, denoted as $Mg(1)O_6$ and $Mg(2)O_6$. They connect in pairs through corner sharing to form $Mg(1)Mg(2)O_{11}$ dimers, and align along *b* axis. P atoms are situated in four kinds of tetrahedral sites, which connect to form diphosphates $P(1)O_3$-O(4)-$P(2)O_3$ and $P(3)O_3$-O(11)-$P(4)O_3$. These diphosphates are interconnected with $Mg(1)Mg(2)O_{11}$ dimers by corner sharing or edge sharing, to form a 3 dimentional $[Mg(P_2O_7)]$ framework. Specifically, the $P(3)O_3$-O(11)-$P(4)O_3$ diphosphate groups connect $Mg(1)Mg(2)O_{11}$ dimers by exclusively corner sharing manner, whereas the $P(1)O_3$-O(4)-$P(2)O_3$ groups through both corner sharing and edge sharing.

Inside the 3-D $[Mg(P_2O_7)]$ framework, four crystallographic Na sites are located. Besides the fully occupied Na(2) and Na(3) sites, Na(1) site is partially substituted by Mg (Na/Mg = 0.82/0.18), and Na(4)/Na(5)/Na(6)/Na(7) are 4 split-atom sites used to reproduce the positional disorder of Na.

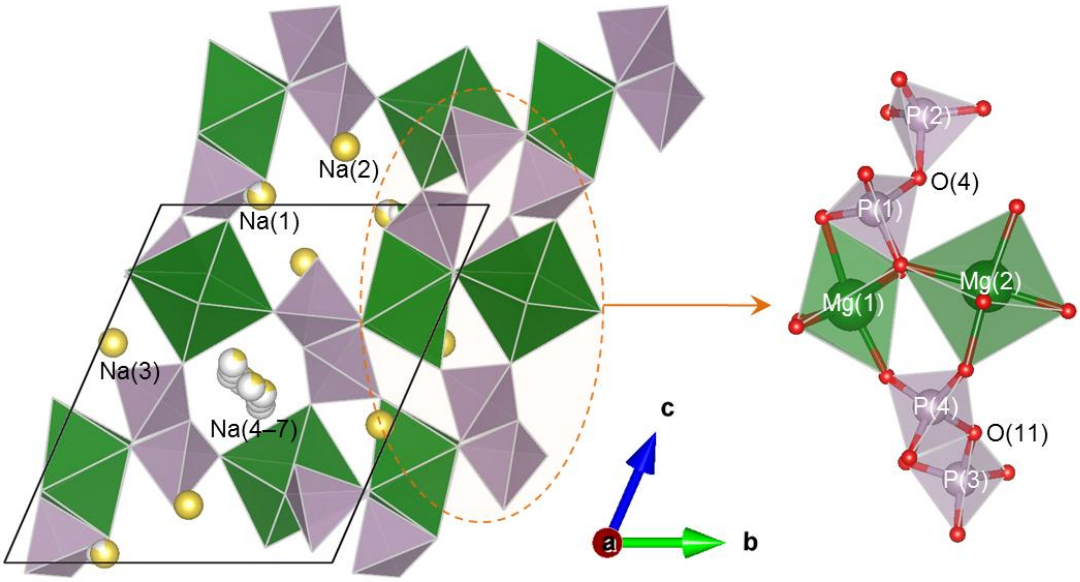

Figure 4.8 Crystal structure of $Na_{1.82}Mg_{1.09}P_2O_7$. MgO_6 octahedra (green) and PO_4 (light purple) are interconnected to form a 3D framework, where Na (yellow) are located. Na(1) site is substituted with Mg, the ratio of Na/Mg equals to 0.82/0.18; Na(4-7) sites are 4 sub-sites for reproducing the positional disorder.

4.3.3 Ionic conductive properties

The variation of AC conductivity of $Na_{1.82}Mg_{1.09}P_2O_7$ *versus* temperature is shown in Fig. 4.9. The insert Nyquist plot was measured at 533 K, and depicted as an example. A Warburg tail at low frequency indicates the capacitance of blocking electrodes. This is typical behavior for ionic conductors with ionic blocking electrodes. Therefore, $Na_{1.82}Mg_{1.09}P_2O_7$ is an ionic conductor. The semi-circle part at high frequency was fitted with an $R_1(R_2Q)$ equivalent circuit, which is depicted at the bottom of Fig. 4.9. R_1 represents shift of the initial point of impedance arc from zero, and can be assigned to the contact resistance of the sample pellet with coated electrodes, R_2 is the sum of the grain boundary and bulk resistance, and Q is a constant phase element (CPE),

responding to properties of the sample, *i.e.* homogeneity in the sample. The resistance of the sample R equals to $R_1 + R_2$. Variation of the ionic conductivity with temperature is well consistent to the Arrhenius expression, $\sigma T = \sigma_0 \exp(-E_a/k_B T)$, where σ_0 is a pre-exponential factor, E_a the activation energy, and k_B the Boltzmann constant. Thus, an activation energy of 0.77 eV is obtained.

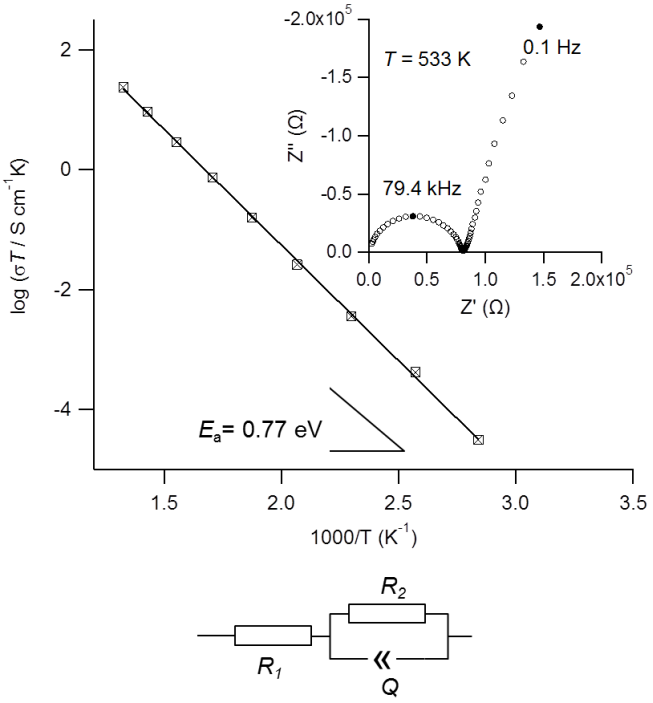

Figure 4.9 Arrhenius plot log(σT) *versus* 1000/T in $Na_{1.82}Mg_{1.09}P_2O_7$. Inset is the Nyquist plot at 533 K.

For comparison, Table 4.4 summarizes the activation energy and ionic conductivity at 573 K in the present work together with related results from the literatures. There is not previous report for conduction properties of crystalline $Na_{1.82}Mg_{1.09}P_2O_7$ sample, therefore only similar data from glassy $Na_{1.82}Mg_{1.09}P_2O_7$ and $Na_7Na_{4.5}(P_2O_7)_4$ are used for comparison. All the samples have the similar ionic conductivity values at 573 K, but are much diverse in the activation energies. In detail,

crystalline $Na_{1.82}Mg_{1.09}P_2O_7$ sample in the present work shows the lowest activation energy, slightly below that of glassy sample[14], whereas $Na_7Na_{4.5}(P_2O_7)_4$ samples show significantly higher E_a values (≈1 eV). Finally, although conduction properties of the crystalline $Na_{1.82}Mg_{1.09}P_2O_7$ sample are little better, but still far from those of a good ionic conductor.

Table 4.4 Ionic conductivity at 573 K and activation energy data for $Na_{1.82}Mg_{1.09}P_2O_7$ and related compounds

Sample	$\sigma_{573\,K}$ (S/cm)	E_a (eV)	Reference
$Na_7Mg_{4.5}(P_2O_7)_4$ (crystalline)	3.89×10^{-7}	1.115	P. Znášik *et al.*[12]
$Na_7Mg_{4.5}(P_2O_7)_4$ (glassy)	2.11×10^{-6}	0.995	P. Znášik *et al.*
$Na_{1.82}Mg_{1.09}P_2O_7$ (glassy)	8.91×10^{-6}	0.85	N. Dridi *et al.*[14]
$Na_{1.82}Mg_{1.09}P_2O_7$ (crystalline)	9.30×10^{-6}	0.77	The present work[20]

4.3.4 Understanding of Na disorder

Positional disorder is frequently found in good ionic conductors, to understand the limited ionic conduction properties in $Na_{1.82}Mg_{1.09}P_2O_7$, a close investigation on Na disorder was conducted. Fig. 4.10 shows the temperature dependences of the atomic displacement parameters of Na. Compared to those at Na(2) and Na(3) sites, Na atoms at Na(1) site show highly localized, with lower and more temperature insensitive atomic displacement parameters. This is because that Mg is statistically substituted at Na(1) site. There are significant overlaps of Na displacement among Na(4)/Na(5)/Na(6)/Na(7) sub-sites, therefore accurate *B* value at each sub-site is difficult to deduce. Instead, an average value for the four sub-sites was calculated. As-obtained *B* value increases from

1.12 Å^2 (300 K) to 2.61 Å^2 (773 K), showing a similar curve to that at Na(1) site and therefore also insensitive to temperature variation. This temperature-insensitive *B* at Na(4)/Na(5)/Na(6)/Na(7) indicates that positional disorder of Na may be static, and the diffuse distribution of Na cage is actually a result of a superposition of local displacements of Na.

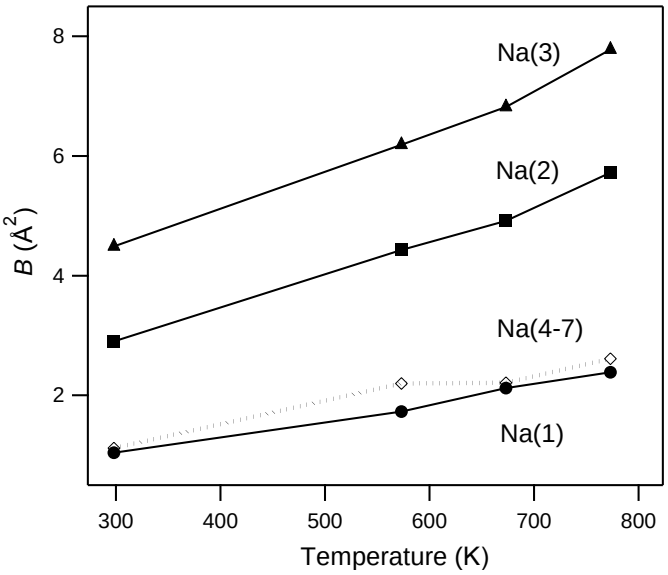

Figure 4.10 Temperature dependences of atomic displacement parameters of Na.

The static disorder hypothesis can be understood with a defect induced disorder model (Fig. 4.11). With a defect free and ideal composition, $Na_2MgP_2O_7$ should have a well ordered Na arrangement, where two Na ions are located at one side of each anisotropic Na cage due to an intra-cage Na-Na electrostatic repulsion. The present compound, $Na_{1.82}Mg_{1.09}P_2O_7$, contains 18% of Na vacancy in each Na cage. This vacancy decreases the Na-Na electrostatic repulsion, and leads to large intra-cage displacement of the left Na ion toward the lowest-energy position in the cage, together with displacement of Na ions in adjacent cages. Superimposing these displacements

over the whole crystal through XRD leads to a version of diffuse Na distribution in the Na cage.

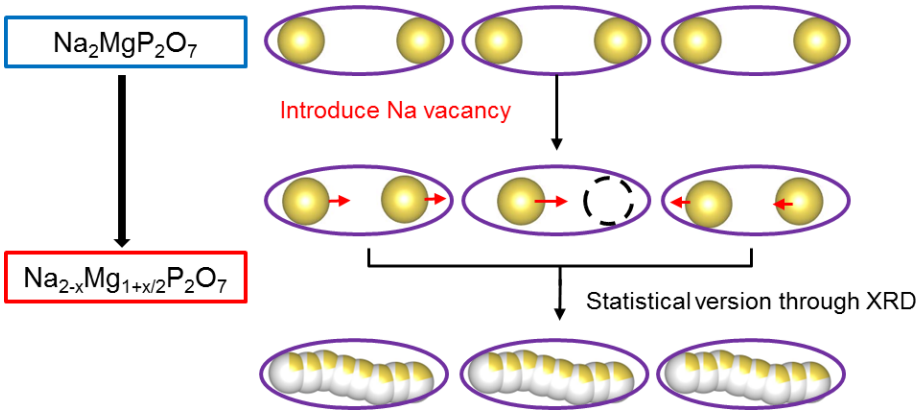

Figure 4.11 Schematic of defect induced disorder formation in the Na cage. Purple elliptic circles represent the Na cages for Na diffuse distribution.

4.3.5 Bond valence sum (BVS) maps

In order to quantify the Na site potential, the BVS map for Na in the present anion framework was calculated. BVS calculation has been widely applied to model site potential and ion diffusion pathways in various compounds,[21–23] the bond valence of each cation-anion pair s_{ij} is calculated as:

$$s_{ij} = \exp(\frac{R_0 - R_{ij}}{b})$$

where R_0 and b are tabulated empirical parameters[24] and equal to 1.803 and 0.37 for the Na^+-O^{2-} pair, respectively; R_{ij} represents the bond length of Na(i)-O(j). The bond valence sum value for site i:

$$V_i = \sum_j s_{ij}$$

The difference between V_i and the ideal BVS value V_{ideal} *is*

$$|\Delta V| = |V_i - V_{ideal}|$$

in which V_{ideal} equals to 1 for the Na case. $|\Delta V|$ gives a standard of positional suitability for Na ions. Smaller $|\Delta V|$ value corresponds to the more stable position for Na, thus the interconnection among these stable position indicate possible Na ion diffusion paths. In contrast, the positions with larger $|\Delta V|$ are associated with bottlenecks for diffusion of Na ion.

The $|\Delta V|$ value was calculated over whole space of the unit cell with a grid size of 0.2×0.2×0.2 $Å^3$, and the results for RT structure are visualized in Fig. 4.12. Two isosurfaces with $|\Delta V|$ = 0.1 (pink) and 0.3 (green) are depicted. They enclose the region with $|\Delta V|$ lower than the specified values. The pink isosurface distributes only in the separated regions around Na(2) and Na(3) sites, confirming the suitability of these sites for Na ions. Na(1) and sub-sites Na(4)/Na(5)/Na(6)/Na(7) have slightly higher $|\Delta V|$, and around the outside of the pink isosurface. These results are compatible with the fact that Mg substitution and static Na disorder exist. Within the green isosurface where $|\Delta V|$ = 0.3, diffuse distribution of Na consists the Na cages [denoted as Na(7)/Na(6)/Na(5)/Na(4)/ Na(4)/Na(5)/Na(6)/Na(7)]. However, the cages are separated from each other by this isosurface. It highlights that migration bottlenecks exist between neighboring Na cages. These bottlenecks impede Na ion migration, and lead to the low ion conductivity in $Na_{1.82}Mg_{1.09}P_2O_7$. Besides, connections between the Na cages and Na(2) or Na(3) sites are enclosed in the isosurface with $|\Delta V|$ = 0.3, indicating that the other possible Na diffusion channels. Therefore, $Na_{1.82}Mg_{1.09}P_2O_7$ shows a 3 dimensional diffusion channels for Na ions. The Empirical force field calculation[20] results show the favorable direction is along the Na cages with an energy barrier of 0.4 eV, and the other two directions to Na(2) and Na(3) sites have a little higher energy

barriers of 0.6 eV. This calculation results confirm the 3-D diffusion channels in $Na_{1.82}Mg_{1.09}P_2O_7$.

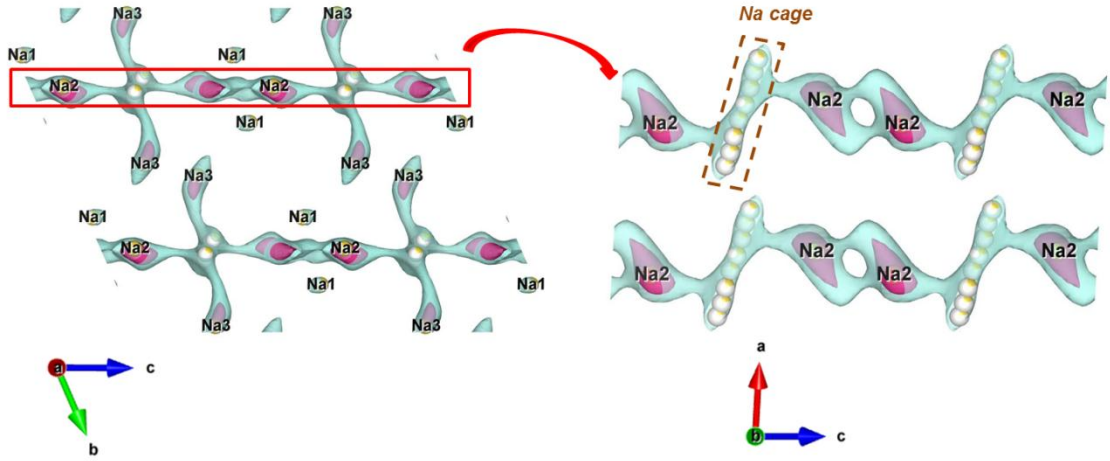

Figure 4.12 Isosurface of bond valence sum deviation ($|\Delta V|$) for Na in $Na_{1.82}Mg_{1.09}P_2O_7$, based on the structure at 300 K. The green isosurface corresponds to positions with $|\Delta V|$ = 0.3, and the pink isosurface to that of $|\Delta V|$ = 0.1.

Additionally, Na(1) sites is isolated from the above isosurfaces. It indicates that Na in the Na(1) site is immobile. This conclusion is consistent to the reported structure in the desodiated $NaFeP_2O_{7,}$[7] in which the occupancies at Na(2), Na(3) and Na cage sites decrease with the desodiation from $Na_2FeP_2O_7$, but that at Na(1) site keeps constant. These facts confirm 3-D Na ion diffusion channels through Na(2), Na(3) and Na cage sites in this structure type.

4.3.6 Na ion diffusion comparison between $Na_{2-x}Mg_{1+x/2}P_2O_7$ and $Na_{2-x}Fe_{1+x/2}P_2O_7$

Although $Na_{2-x}M_{1+x/2}P_2O_7$-type structures have the similar three dimensional conduction mechanism, the specific structure according to different *M* atoms would lead to the variation of ionic conduction properties. Thus, using $Na_{2-x}Mg_{1+x/2}P_2O_7$ to model the $Na_{2-x}Fe_{1+x/2}P_2O_7$ system has some limitation.

BVS maps with $|\Delta V|$ = 0.4 on the isosurface for $Na_{2-x}Mg_{1+x/2}P_2O_7$ and $Na_{2-x}Fe_{1+x/2}P_2O_7$ are shown as Fig. 4.13 (a), (b). The favored migration path (path A) along Na cages is enclosed in the isosurface for $Na_{2-x}Fe_{1+x/2}P_2O_7$, but interrupted in the case of $Na_{2-x}Mg_{1+x/2}P_2O_7$. Enclosing the path A of $Na_{2-x}Mg_{1+x/2}P_2O_7$ needs an isosurface with $|\Delta V| \geq 0.6$. This kind of difference can be understood from the size of bottlenecks along path A (denoted as a black circle in Fig. 4.13). The bottleneck consists of two P_2O_7 dimers separated by MO_6 (*M* = Mg, Fe) octahedra (Fig. 4.13c). The average length of the Fe-O bonds (≈ 2.16 Å) is longer than that of the Mg-O bonds (≈ 2.10 Å), and this length difference accounts for ca. 0.1~0.2 Å difference in size of the bottleneck, which is indicated from d_1 and d_2 value in Fig. 4.13. Consequently, the Na ionic conduction in $Na_{2-x}Fe_{1+x/2}P_2O_7$ is expected to be accelerated, compared to that in $Na_{2-x}Mg_{1+x/2}P_2O_7$. A recent theoretical study[25] reported that the lowest energy barrier (along path A) in $Na_2FeP_2O_7$ is 0.33 eV, consistent with the present discussion. Additionally, they also concluded that Na ion diffusion in $Na_2FeP_2O_7$ is of 3-D diffusion nature and the path A along *a* axis is the favored diffusion path.

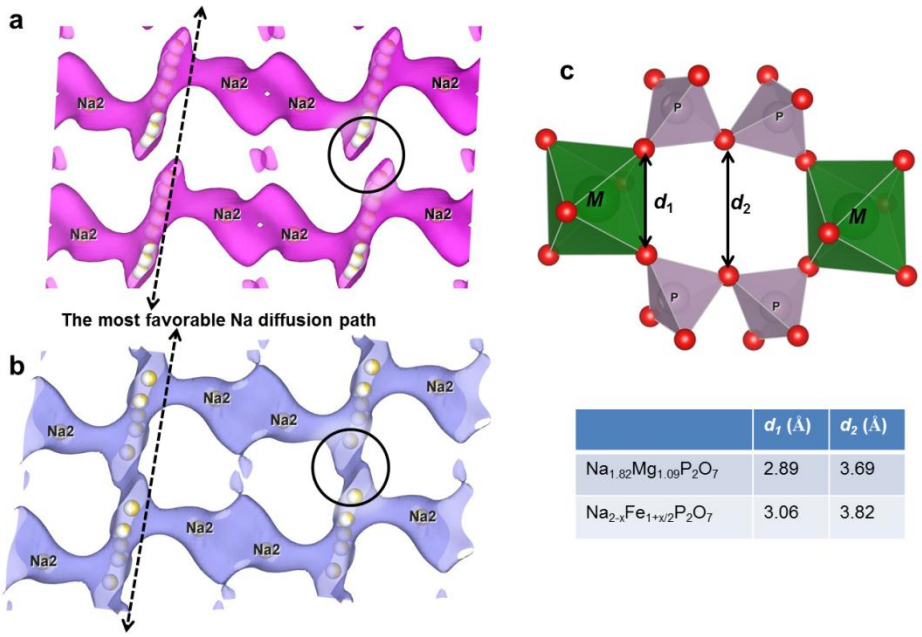

	d_1 (Å)	d_2 (Å)
$Na_{1.82}Mg_{1.09}P_2O_7$	2.89	3.69
$Na_{2-x}Fe_{1+x/2}P_2O_7$	3.06	3.82

Figure 4.13 BVS isosurface with $|\Delta V|$ = 0.4 in $Na_{1.82}Mg_{1.09}P_2O_7$ (a) and $Na_{2-x}Fe_{1+x/2}P_2O_7$ (b). Bottlenecks between the adjacent Na cages are marked with black circles, and the details are shown in (c), together with the table of sizes (d_1 and d_2) of cavities surrounded by the bottlenecks.

4.4 Conclusion

In summary, nonstoichiometric $Na_{1.82}Mg_{1.09}P_2O_7$ has been synthesized by solid state method. The crystal structure and ionic conductivity have been investigated in a wide temperature range (300 K~773 K). With bond valance sum calculation, Na ion conduction mechanism has been elaborated. The main results are listed as follows:

(1) Diffuse distribution of Na was observed at sub-sites Na(4)/Na(5)/Na(6)/Na(7), which consist of Na cages aligning along [100]. The average atomic displacement parameter at Na(4)/Na(5)/Na(6)/Na(7) shows weak temperature dependence. It indicates static disorder inside the Na cages, and a defect induced disorder model was proposed.

(2) The ionic conductivity of crystalline $Na_{1.82}Mg_{1.09}P_2O_7$ sample has been firstly reported, which equals to 9.30×10^{-6} S/cm at 573 K with an activation energy of 0.77 eV. Using the Arrhenius equation, a room-temperature ionic conductivity of 1.10×10^{-11} S/cm was obtained.

(3) Based on bond valence sum results, 3-D Na diffusion channels in this crystal type have been proven. Specifically, the migration along the Na cages has been verified as the favored path. However, bottlenecks exist between neighbor cages which impede Na ion migration, despite the highly favorable positional disorder of Na within the cages.

(4) The Na migration mechanism can shed light on other isostructural $Na_{2-x}M_{1+x/2}P_2O_7$-type compounds, i.e. $Na_{2-x}Fe_{1+x/2}P_2O_7$, one promising cathode material for Na-ion batteries.

4.5 Reference

(1) Kim, S.-W.; Seo, D.-H.; Ma, X.; Ceder, G.; Kang, K. *Adv. Energy Mater.* **2012**, *2*, 710–721.

(2) Ellis, B. L.; Nazar, L. F. *Curr. Opin. Solid State Mater. Sci.* **2012**, *16*, 168–177.

(3) Palomares, V.; Serras, P.; Villaluenga, I.; Hueso, K. B.; Carretero-González, J.; Rojo, T. *Energy Environ. Sci.* **2012**, *5*, 5884–5901.

(4) Grosjean, C.; Miranda, P. H.; Perrin, M.; Poggi, P. *Renew. Sustain. Energy Rev.* **2012**, *16*, 1735–1744.

(5) Poole, D.; Argent, B. B.; Sharifi, V. N.; Swithenbank, J. *Fuel* **2008**, *87*, 1318–1333.

(6) Barpanda, P.; Ye, T.; Nishimura, S.; Chung, S.-C.; Yamada, Y.; Okubo, M.; Zhou, H.; Yamada, A. *Electrochem. commun.* **2012**, *24*, 116–119.

(7) Barpanda, P.; Liu, G.; Ling, C. D.; Tamaru, M.; Avdeev, M.; Chung, S.-C.; Yamada, Y.; Yamada, A. *Chem. Mater.* **2013**, *25*, 3480–3487.

(8) Kim, H.; Shakoor, R. A.; Park, C.; Lim, S. Y.; Kim, J.-S.; Jo, Y. N.; Cho, W.; Miyasaka, K.; Kahraman, R.; Jung, Y.; Choi, J. W. *Adv. Funct. Mater.* **2013**, *23*, 1147–1155.

(9) Ha, K.-H.; Woo, S. H.; Mok, D.; Choi, N.-S.; Park, Y.; Oh, S. M.; Kim, Y.; Kim, J.; Lee, J.; Nazar, L. F.; Lee, K. T. *Adv. Energy Mater.* **2013**, *3*, 770–776.

(10) Majling, J.; Hanic, F. *J. Solid State Chem.* **1973**, *7*, 370–373.

(11) Hanic, F.; Žák, Z. *J. Solid State Chem.* **1974**, *10*, 12–19.

(12) Znášik, P.; Hinduliakova, I.; Majlin, J. *Solid State Ionics* **1993**, *60*, 313–317.

(13) Erragh, F.; Boukhari, A.; Abraham, F.; Elouadi, B. *J. Solid State Chem.* **2000**, *152*, 323–331.

(14) Dridi, N.; Boukhari, A.; Reau, J. M. *Solid State Ionics* **1998**, *110*, 131–136.

(15) Toraya, H.; Hibino, H.; Ohsumi, K. *J. Synchrotron Radiat.* **1996**, *3*, 75–83.

(16) Yashima, M.; Tanaka, M.; Oh-uchi, K.; Ida, T. *J. Appl. Crystallogr.* **2005**, *38*, 854–855.

(17) Yashima, M.; Oh-uchi, K.; Tanaka, M.; Ida, T. *J. Am. Ceram. Soc.* **2006**, *89*, 1395–1399.

(18) Momma, K.; Izumi, F. *J. Appl. Crystallogr.* **2011**, *44*, 1272–1276.

(19) Parthé, E.; Gelato, L. M. *Acta Crystallogr.* **1984**, *A40*, 169–183.

(20) Liu, G.; Nishimura, S.; Chung, S. C.; Fujii, K.; Yashima, M.; Yamada, A. *J. Mater. Chem. A* **2014**, *2*, 18353–18359.

(21) Adams, S. *Solid State Ionics* **2000**, *136-137*, 1351–1361.

(22) Avdeev, M.; Sale, M.; Adams, S.; Rao, R. P. *Solid State Ionics* **2012**, *225*, 43–46.

(23) Mazza, D. *J. Solid State Chem.* **2001**, *156*, 154–160.

(24) Brown, I. D.; Altermatt, D. *Acta Crystallogr. Sect. B* **1985**, *41*, 244–247.

(25) Clark, J. M.; Barpanda, P.; Yamada, A.; Islam, M. S. *J. Mater. Chem. A* **2014**, *2*, 11807–11812.

5 Enhanced capacity of ordered $Na[Na_{1/3}Ru_{2/3}]O_2$ for a cathode material of sodium-ion batteries

5.1 Introduction

Sodium-ion batteries have attracted much attention recently, because of their potential for large-scale applications: high power and less expensive batteries can be realized by utilizing abundant and polarizable sodium ion as a mobile charge carrier. One of the main obstacles to realize high performance sodium-ion batteries is a low specific capacity of the electrode materials. In particular, the present set of cathode materials including sodium transition metal oxides (Na_xMO_2, M = transition metals) and polyanionic compounds ($Na_xM_y(X_nO_m)z$, X = P, S, V…) deliver the specific capacities of 100−180 mAh/g associated with the redox of M,[1–4] which are relatively lower than those of Li-ion cathode materials (140−250 mAh/g). Furthermore, the Na-ion cathode materials generally operate at lower potential than the Li-ion cathode materials, leading to the lower energy density. Thus, of particular importance is to develop novel Na-ion cathode materials with a high capacity as well as a high operating potential.

Utilization of an oxygen redox in sodium transition metal oxides is a potentially effective strategy for struggling with the sodium-ion cathode problem. Contribution of oxygen orbital to redox reaction has been recognized for a long time as an obvious consequence for a M-O covalent character.[5,6] Very recently, clear and systematic experimental evidences were given by using the Li excess transition metal oxides, *i.e.*, Li_2MO_3 (or $Li[Li_{1/3}M_{2/3}]O_2$).[7,8] In general, the crystal structure of Li_2MO_3 is described as alternative stacking of Li and $[Li_{1/3}M_{2/3}]$ layers in the array of cubic close packed oxygen ions, providing a generalized formula of $Li[Li_{1/3}M_{2/3}]O_2$. In the $[Li_{1/3}M_{2/3}]$ layer,

Li and *M* ions are arranged in an ordered honeycomb fashion. In ref. 8, a series of $Li[Li_{1/3}(Ru_{1-y}Sn_y)_{2/3}]O_2$ exhibits a potential plateau at 4.3 V vs. Li/Li^+ regardless of the fraction *y* of the redox-inactive Sn^{4+}, indicating the oxygen redox. Owing to the additional capacity associated with the oxygen redox, $Li[Li_{1/3}(Ru_{0.75}Sn_{0.25})_{2/3}]O_2$ delivers a high capacity above 200 mAh/g with a relatively high average potential of 3.6 V vs. Li/Li^+.

We have targeted to adopt the oxygen redox chemistry in the Na-ion cathode materials with an eye to the more stable nature of layered structure by the larger contrast in ionic radii of transition metal ions and sodium ions. This may lead to more efficient utilization of oxygen redox reaction without destroying the framework structure. Our group has recently reported the electrochemical properties of Na excess transition metal oxide $Na[Na_{0.23}Ru_{0.77}]O_2$.[9] However, despite the Na excess composition similar to $Li[Li_{1/3}M_{2/3}]O_2$, $Na[Na_{0.23}Ru_{0.77}]O_2$ delivers only 140 mAh/g associated with 0.7 Na-ion extraction. Importantly, the potential profile shows no potential plateau at high voltage. Therefore, unlike the Li system, the oxygen redox is not available in $Na[Na_{0.23}Ru_{0.77}]O_2$.

A possible origin for the significant difference in electrochemical properties is the cation arrangement in the [Na*M*] layer. While the cation arrangement in the [Li*M*] layer of $Li[Li_{1/3}(Ru_{1-y}Sn_y)_{2/3}]O_2$ orders in a honeycomb fashion, that in the [Na*M*] layer of $Na[Na_{0.23}Ru_{0.77}]O_2$ disorders maybe due to the decreased content of Na.

In this chapter, a stoichiometric $Na[Na_{1/3}Ru_{2/3}]O_2$ with more Na in the [NaRu] layer was obtained through a different synthetic method, which realizes an enhanced capacity.

5.2 Research methods

Material Synthesis: Two kinds of solid state methods have been utilized in this chapter, direct synthesis (DS) and thermal decomposition (TD). In the former method, stoichiometric amounts of Na_2CO_3 and RuO_2 were weighted and added into planetary ball-milling pot with 50 mL acetone. After mixed at 400rpm for 4h, the precursor was vacuumed whole night to remove the acetone and pressed into cylindrical pellets for sintering at 1123 K for 12 h in Ar atmosphere. Pure black product was obtained and transferred into Ar glovebox without exposure to air.

For the TD method, Na_2RuO_4 was prepared at first. Stoichiometric Na_2O_2 and RuO_2 were mixed by a hand milling in Ar atmosphere and pressed into pellets by a hand pressure. Then, the pellets were calcined in O_2 atmosphere at 923 K for 12h. After cooling down to room temperature, the obtained Na_2RuO_4 pellets were fine grounded and characterized by Lab XRD. Then, the Na_2RuO_4 powders were pressed into pellets again and sintered in Ar atmosphere at 1123 K for 2-40h. Thermal decomposition of Na_2RuO_4 occurs during this process, and $Na[Na_{1/3}Ru_{2/3}]O_2$ was obtained as the final product.

Laboratory X-ray diffraction: Powder X-ray diffraction was performed with a Bruker AXS D8 ADVANCE powder diffractometer using Co-Kα radiation (λ_1 = 1.78897 Å), or a Rigaku RINT-TTR III powder diffractometer with Cu-Kα radiation (λ_1 = 1.54056 Å). As $Na[Na_{1/3}Ru_{2/3}]O_2$ and Na_2RuO_4 are both air sensitive, all the samples were measured in the protection of Ar atmosphere.

Electrochemical characterization: $Na[Na_{1/3}Ru_{2/3}]O_2$ powders, acetylene carbon black and polyvinylidene (PVDF) were mixed in a weight ratio of 8:1:1 and grounded homogenously. Several drops of N-methyl pyrrolidone (NMP) were added to make a

slurry which is then coated on an Al film as the cathode for Na half-cells. The thickness of coating was 100 μm. After a simply drying, the as-obtained cathode film was cut into disks with a diameter of 12 mm and conducted overnight drying in vacuum at 393 K. Then, 2032-type coin cells were assembled with the disk as the cathode, Na metal as the anode, and 1M $NaPF_6$ in Ethylene carbonate (EC)/ Diethyl carbonate (DEC) (1:1) as the electrolyte. 2 vol% of fluoroethylene carbonate (FEC) was utilized as additive in the electrolyte. All the processes including mixing, coating and battery assembly were conducted in Ar glovebox. The cells were measured in the voltage range of 1.5~4 V at a rate of 27 mA/g.

5.3 Results and discussion

5.3.1 $Na[Na_{1/3}Ru_{2/3}]O_2$ obtained from thermal decomposition (TD) of Na_2RuO_4

To synthesize the stoichiometric $Na[Na_{1/3}Ru_{2/3}]O_2$, a thermal decomposition (TD) method was utilized. This method was firstly proposed by Mogare et al.[10] and can be described with the following reaction equations

$$Na_2O_2 + RuO_2 \rightarrow Na_2RuO_4 \ (O_2, 923\ K)$$

$$2Na_2RuO_4 \rightarrow 3Na[Na_{1/3}Ru_{2/3}]O_2 + O_2 \ (Ar, 1123\ K)$$

Fig. 5.1 (a) shows the XRD patterns of products from the TD method with different sintering times. The pattern of disordered $Na[Na_{0.23}Ru_{0.77}]O_2$ from the directly synthesis (DS) method is also appended for comparison. Different to the DS sample, superstructure peaks appear at the 2θ of ca. 22° in the TD samples. The intensity of the superstructure peaks increases with extending the sintering time from 2h to 40h.

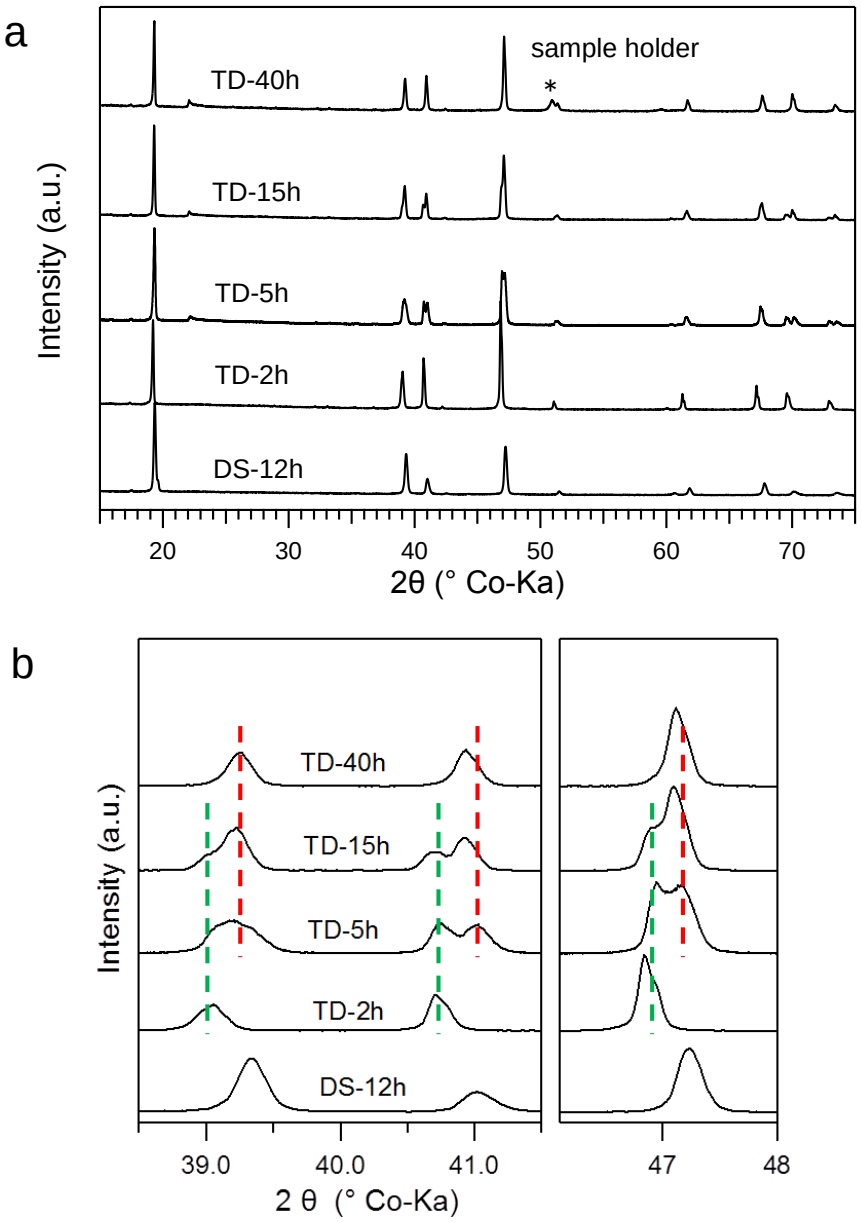

Figure 5.1 (a) XRD patterns of thermal-decomposition (TD) $Na[Na_{1/3}Ru_{2/3}]O_2$ samples, compared with directly synthesized (DS) sample. Asterisk denotes the signal from sample holder. The superstructure peaks at ca. 22° appear only in the TD samples. The XRD patterns in 2θ ranges of 38.5~41.5° and 46~48° are enlarged in (b).

In Fig. 5.1(b), the XRD patterns in the range of 38 ~ 48° are enlarged. With extending the sintering time, intensities of the diffraction peaks marked with green

broken lines decrease and intensities of those marked with red broken lines increase. This clearly shows a phase transformation during thermal decomposition from 2h to 40h. The compound after 40h sintering has the lattice parameters (a = 3.11809(8), c = 16.0035(9), V= 134.748(10)) similar to that of the DS sample (a = 3.11245(12), c = 15.9537(15), V= 133.844(11)), and was used in the following experiments.

5.3.2 Crystal structure description

The appearance of superstructure peaks of (020), (110) and $(1\,\bar{1}\,\bar{1})$ denoted in the *C*2/c space group is a good sensor to detect the honeycomb-like order in samples. As mentioned above, the superstructure peaks can be only detected in the Lab XRD patterns of TD samples. To confirm this fact, Synchrotron XRD patterns of the TD-Na$[Na_{1/3}Ru_{2/3}]O_2$ sample (TD-40h) and the DS-Na$[Na_{0.23}Ru_{0.77}]O_2$ sample have been collected and are depicted in Fig. 5.2. Compared to DS-Na$[Na_{0.23}Ru_{0.77}]O_2$, TD-Na$[Na_{1/3}Ru_{2/3}]O_2$ shows significant superstructure peaks. This confirms the honeycomb-like order in TD-Na$[Na_{1/3}Ru_{2/3}]O_2$, but disorder arrangement in DS-Na$(Na_{0.23}Ru_{0.77})O_2$. Nonetheless, the superstructure peaks are seriously overlapped, possibly due to the intra-layer defects or stacking defects.[11,12]

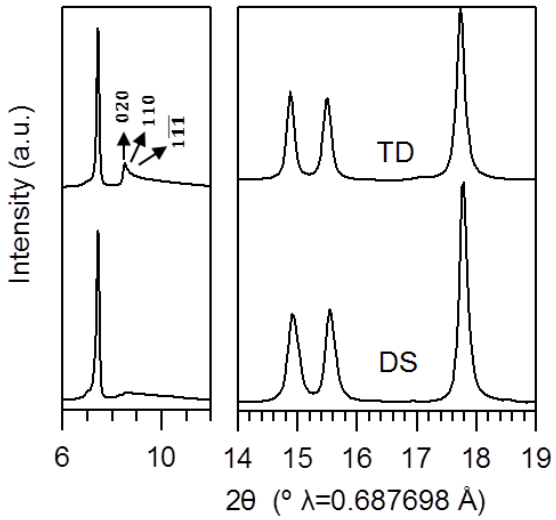

Figure 5.2 Synchrotron powder XRD patterns of the DS-Na[$Na_{0.23}Ru_{0.77}$]O_2 and the TD-Na[$Na_{1/3}Ru_{2/3}$]O_2 samples. The superstructure peaks (020) (110) and (1 $\bar{1}$ $\bar{1}$) are denoted in a *C*2/c symmetry.

To clarify the crystal structures, ordered and disordered structure models[10] are depicted in Fig. 5.3. Both the layered structures are stacked by alternate Na layer and [$Na_{1/3}Ru_{2/3}$] layer. The ordered structure takes a *C*2/c space group. Na and Ru ions are located in a honeycomb-like lattice in the [$Na_{1/3}Ru_{2/3}$] layer (Fig. 5.3 left). Each Na ion is surrounded by six Ru ions, whereas each Ru ion is connected with three Na and three Ru ions. The total ratio of Na and Ru ions is 1:2. On the other hand, the fully disordered structure is represented in an *R*-3m space group. In the disordered Na[$Na_{0.23}Ru_{0.77}$]O_2, each site in the [$Na_{0.23}Ru_{0.77}$] layer has an uniform occupancy of 0.23 for Na and of 0.77 for Ru. In average, one Ru site is surrounded with 1.38 Na and 4.62 Ru ions. Consequently, Ru ions are separated from each other more efficiently in the ordered honeycombic arrangement.

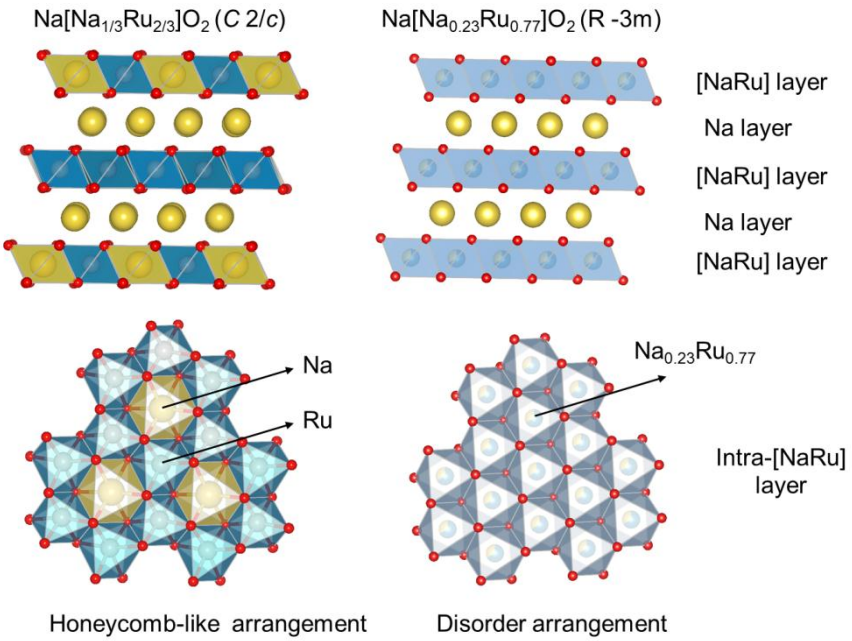

Figure 5.3 Schematic representation of the crystal structures of ordered $Na[Na_{1/3}Ru_{2/3}]O_2$ (left) and disordered $Na[Na_{0.23}Ru_{0.77}]O_2$ (right). A honeycomb-type arrangement of Na and Ru ions in the [NaRu] layer is formed for the ordered one.

5.3.3 Electrochemical performance valuation

Fig. 5.4 depicts galvanostatic charge-discharge curves for the disordered DS-$Na[Na_{0.23}Ru_{0.77}]O_2$ and ordered TD-$Na[Na_{1/3}Ru_{2/3}]O_2$. The two phases show much different electrochemical performance. DS-$Na[Na_{0.23}Ru_{0.77}]O_2$ delivers a discharge capacity of 135 mAh/g, corresponding to the following redox reaction,

$$Na[Na_{0.23}Ru_{0.77}]O_2 \leftrightarrows 0.7Na^+ + 0.7e^- + Na_{1-x}[Na_{x-0.47}Ru_{0.77}]O_2$$

Except one small plateau at 2.6 V, the charge-discharge curves show thoroughly sloping trend, confirming the solid solution process reported by Tamaru et al.[9]

In contrast, the ordered TD-$Na[Na_{1/3}Ru_{2/3}]O_2$ sample delivers an enhanced capacity of 182 mAh/g, corresponding to 0.9 Na extraction. The electrochemical reaction is written as,

$$Na[Na_{1/3}Ru_{2/3}]O_2 \leftrightarrows 0.9Na^+ + 0.9e^- + Na_{1-x}[Na_{x-0.57}Ru_{2/3}]O_2.$$

Three plateaus are observed on the charge curve. The former two at low voltage show well reversibility on the following discharge process; whereas the plateau at ca. 3.6 V only appears on the charge process and large potential hysteresis is observed on the related discharge range.

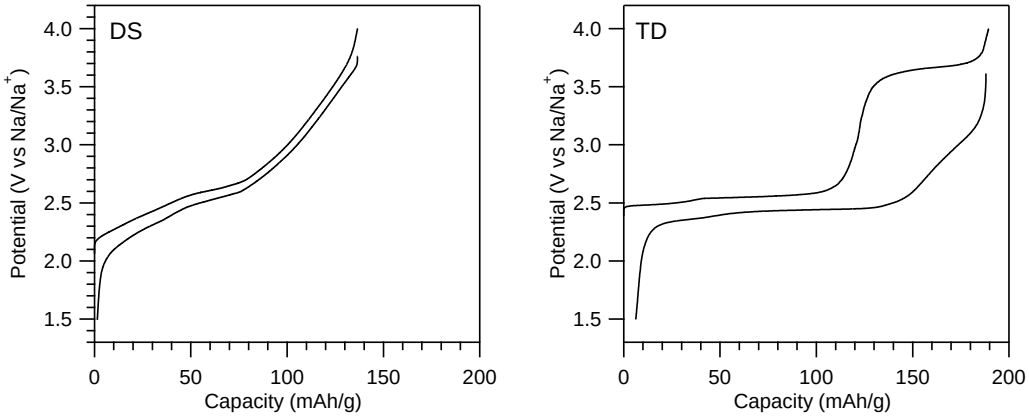

Figure 5.4 Charge-discharge curves of DS-$Na[Na_{0.23}Ru_{0.77}]O_2$ and TD-$Na[Na_{1/3}Ru_{2/3}]O_2$ samples.

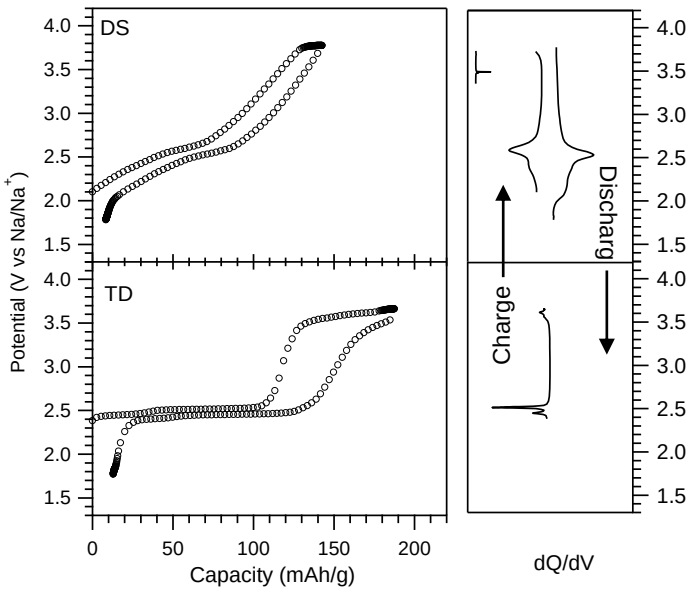

Figure 5.5 The charge-discharge curve measured with GITT method, and as-calculated d*Q*/d*V* curves are depicted on the right.

Then, to precisely analyze the potential difference in these two samples, the charge-discharge curves are collected from Galvanostatic Intermittent Titration Technique (GITT) measurement. The data at each point is recorded after 1h rest of cells. As-collected results are depicted in Fig. 5.5, in which the derivative of the capacity (*Q*) with respect to the potential (*V*), d*Q*/d*V* curves, are also shown. The d*Q*/d*V* peaks are corresponding to plateaus on the charge-discharge curves and can be treated as the redox potential peaks. DS-Na[$Na_{0.23}Ru_{0.77}$]O_2 sample shows one broad d*Q*/d*V* peak at ca. 2.6 V, corresponding to the two-phase range reported previously.[9]

The TD sample has three sharp dQ/dV peaks at 2.45 V, 2.52 V and 3.62 V on the charge process. The former two are reversible in the following discharge and corresponding to the redox reaction of Ru^{5+}/Ru^{4+}. The third plateau at 3.62 V induces the enhanced capacity. Similar plateau at 4.2 V has been reported in Li_2RuO_3[7,8,13] as a

cathode material for Li-ion batteries, and was related to oxygen activation ($O^{2-} \rightarrow O^{-}$ or O_2).

It's of interest that the two Na-Ru-O samples with different degrees of disorder show such large voltage differences during the electrochemical cycling. Previously, different charge-discharge profiles have also been reported for two polymorphs of $LiFeSO_4F$ (tavorite-type and triplite-type) in Li-ion batteries. Chung et al.[14] explained the different Fe^{3+}-Fe^{3+} electrostatic repulsion in the delithiated states as the main inducer to potential variations. They concluded that, the stronger the Fe^{3+}-Fe^{3+} repulsion effect, the more unstable the delithiated state, and then the higher the oxidation potential for Fe^{3+}/Fe^{2+} couple following the definite thermodynamic origin. Due to the high valence of Ru in DS-$Na[Na_{0.23}Ru_{0.77}]O_2$, TD-$Na[Na_{1/3}Ru_{2/3}]O_2$ and their desodiated states, Ru-Ru electrostatic repulsion should be also crucial to the redox potential. In the fully disordered $Na[Na_{0.23}Ru_{0.77}]O_2$ sample, due to the disordered arrangement of Na and Ru in the [NaRu] layer, the extent of cation-cation repulsion effect of Ru-Ru distributes in a wide range. It then results in the dispersion of redox potential as shown in the dQ/dV curve (Fig. 5.5). On the other hand, those sharp plateaus in the ordered $Na[Na_{1/3}Ru_{2/3}]O_2$ sample are consistent with the honeycombic arrangement of Ru and Na sites in the $[Na_{1/3}Ru_{2/3}]$ layer.

As mentioned in the crystal structure description part, the honeycomb-like arrangement can relax Ru-Ru repulsions. This fact can explain the lower average voltage of the ordered TD-$Na[Na_{1/3}Ru_{2/3}]O_2$ sample (~2.5 V for the Ru^{5+}/Ru^{4+} reaction part) than that of the disordered DS-$Na[Na_{0.23}Ru_{0.77}]O_{23}$ sample (~2.8 V). It is also consistent with the recent theoretic prediction that disordered materials must exhibit a higher potential that their ordered analogues.[15]

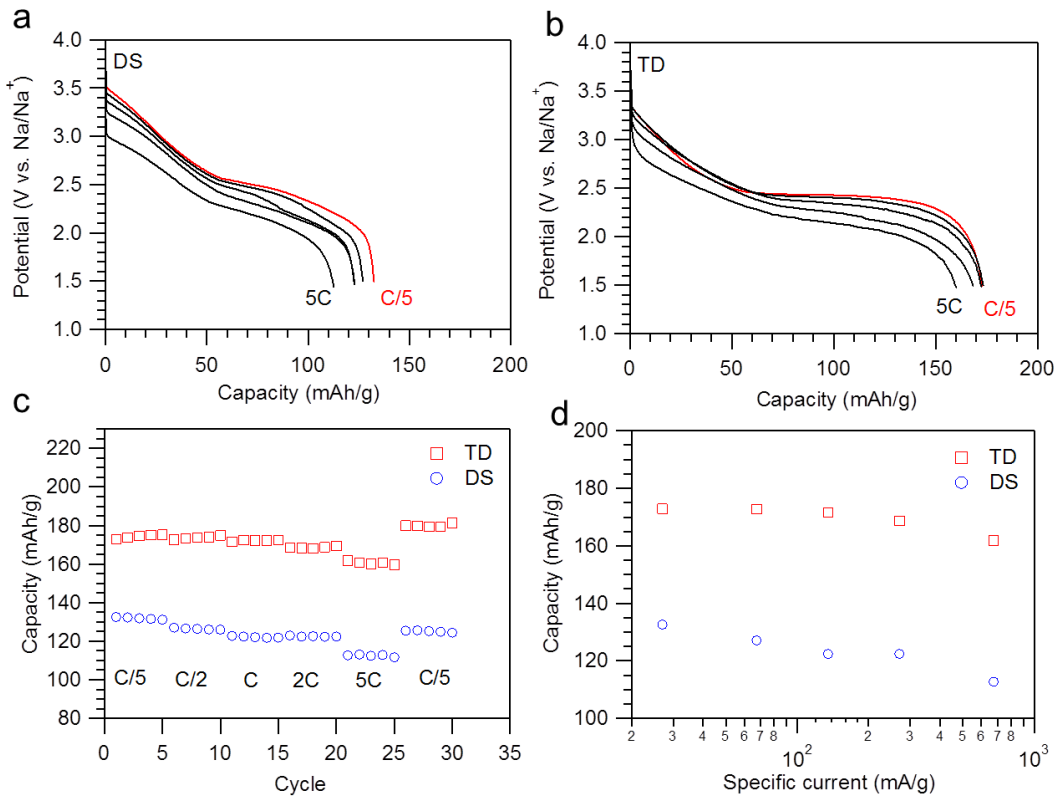

Figure 5.6 Characterization of rate capability for TD-Na[$Na_{1/3}Ru_{2/3}$]O_2 and DS-Na[$Na_{0.23}Ru_{0.77}$]O_2.

Fig. 5.6 depicts the high rate capability results. DS-Na[$Na_{0.23}Ru_{0.77}$]O_2 and TD-Na[$Na_{1/3}Ru_{2/3}$]O_2 samples both have good rate capability. At the discharge rate of 5C (675 mA/g), TD-Na[$Na_{1/3}Ru_{2/3}$]O_2 delivers a capacity of 160 mAh/g and DS-Na[$Na_{0.23}Ru_{0.77}$]O_2 a value of 112 mAh/g. The ordered TD-Na[$Na_{1/3}Ru_{2/3}$]O_2 sample shows a slightly better rate performance, which may be due to the ordered arrangement of Na and Ru in the [NaRu] layer.

5.4 Conclusion

In summary, Na[$Na_{1/3}Ru_{2/3}$]O_2 with honeycomb-like ordering in the [$Na_{1/3}Ru_{2/3}$]

layer has been obtained by thermal decomposition (TD) of Na_2RuO_4. The TD-$Na[Na_{1/3}Ru_{2/3}]O_2$ sample delivers an enhanced capacity of ca. 180 mAh/g, corresponding to ca. 0.9 Na extraction. It is much more competitive than the directly synthesized (DS) $Na[Na_{0.23}Ru_{0.77}]O_2$, which is fully disordered in the [NaRu] layer and only delivers a capacity of 135 mAh/g. The enhanced capacity is related to oxygen activation, which corresponds to the highly hybridization of O 2p and Ru 4d orbitals. Even though this compound is mainly utilized for fundamental research due to the high cost of Ru, the present work provides a direction to design new cathode materials with enhanced capacity for Na-ion batteries.

5.5 Reference

(1) Palomares, V.; Serras, P.; Villaluenga, I.; Hueso, K. B.; Carretero-González, J.; Rojo, T. *Energy Environ. Sci.* **2012**, *5*, 5884–5901.

(2) Han, M. H.; Gonzalo, E.; Singh, G.; Rojo, T. *Energy Environ. Sci.* **2014**, Accepted Manuscript, DOI: 10.1039/C4EE03192J.

(3) Ellis, B. L.; Nazar, L. F. *Curr. Opin. Solid State Mater. Sci.* **2012**, *16*, 168–177.

(4) Yabuuchi, N.; Kubota, K.; Dahbi, M.; Komaba, S. *Chem. Rev.* **2014**, Article ASAP, DOI: 10.1021/cr500192f.

(5) Ceder, G.; Chiang, Y.; Sadoway, D. *Nature* **1998**, *392*, 694–696.

(6) Aydinol, M.; Kohan, a.; Ceder, G.; Cho, K.; Joannopoulos, J. *Phys. Rev. B* **1997**, *56*, 1354–1365.

(7) Sathiya, M.; Ramesha, K.; Rousse, G.; Foix, D.; Gonbeau, D.; Prakash, A. S.; Doublet, M. L.; Hemalatha, K.; Tarascon, J.-M. *Chem. Mater.* **2013**, *25*, 1121–1131.

(8) Sathiya, M.; Rousse, G.; Ramesha, K.; Laisa, C. P.; Vezin, H.; Sougrati, M. T.; Doublet, M.-L.; Foix, D.; Gonbeau, D.; Walker, W.; Prakash, a S.; Ben Hassine, M.; Dupont, L.; Tarascon, J.-M. *Nat. Mater.* **2013**, *12*, 827–835.

(9) Tamaru, M.; Wang, X.; Okubo, M.; Yamada, A. *Electrochem. commun.* **2013**, *33*, 23–26.

(10) Mogare, K. M.; Friese, K.; Klein, W.; Jansen, M. *Zeitschrift für Anorg. und Allg. Chemie* **2004**, *630*, 547–552.

(11) Bréger, J.; Jiang, M.; Dupré, N.; Meng, Y. S.; Shao-Horn, Y.; Ceder, G.; Grey, C. P. *J. Solid State Chem.* **2005**, *178*, 2575–2585.

(12) Boulineau, A.; Croguennec, L.; Delmas, C.; Weill, F. *Solid State Ionics* **2010**, *180*, 1652–1659.

(13) Sarkar, S.; Mahale, P.; Mitra, S. *J. Electrochem. Soc.* **2014**, *161*, A934–A942.

(14) Chung, S. C.; Barpanda, P.; Nishimura, S.-I.; Yamada, Y.; Yamada, A. *Phys. Chem. Chem. Phys.* **2012**, 8678–8682.

(15) Saubanère, M.; Yahia, M. Ben; Lebègue, S.; Doublet, M.-L. *Nat. Commun.* **2014**, *5*, 5559.

6 Summary and outlook

6.1 Summary

This thesis focuses on intercalation cathode materials for Na-ion batteries. There are two main groups of intercalation cathode materials— polyanionic compounds and layered oxides, which are both included in the present work.

Chapter 3 discussed the safety issue on $Na_2FeP_2O_7$ as a cathode material. The desodiated $NaFeP_2O_7$ is found thermally stable up to 873 K, with no decomposition and/or oxygen evolution. Only a polymorphic transition at 837 K from triclinic (P -1) to monoclinic (P 2_1/c) phase was observed. This thermal stability far exceeds those of layered oxides and is at least comparable to other polyanionic cathodes. Combining with low cost, high rate kinetics and moderate voltage, $Na_2FeP_2O_7$ was proven to be a promising candidate for Na-ion battery cathode.

Chapter 4 focused on the ionic conduction properties of $Na_{2-x}M_{1+x/2}P_2O_7$-type materials. Because the valence change of transition metal would introduce undesirable structural imperfections into $Na_{2-x}M_{1+x/2}P_2O_7$ (M = transition metal), i.e. sodium nonstoichiometry and hole defect at the transition metal sites. In order to minimize these contributions to Na ion transport, I chose the redox-inactive Mg analogue, $Na_{2-x}Mg_{1+x/2}P_2O_7$, as a model system. With precise crystal structure obtained from Rietveld refinement of Synchrotron XRD patterns, the ionic conduction mechanism has been elucidated.

Chapter 5 introduced a stoichiometric $Na[Na_{1/3}Ru_{2/3}]O_2$ with honeycomb-like order on the $Na_{1/3}Ru_{2/3}$ slabs as a new cathode material. Its electrochemical performance has been researched in detail as Na ion battery cathode. Interestingly, this compound shows

a high capacity of ca. 180 mAh/g. It is much distinguished from the capacity of ca. 140 mAh/g for the formerly reported $Na[Na_{0.23}Ru_{0.77}]O_2$. Combining with the excellent rate capability, $Na[Na_{1/3}Ru_{2/3}]O_2$ should be a potential cathode material for Na ion batteries. Due to the high price of Ru, $Na[Na_{1/3}Ru_{2/3}]O_2$ might not be applied practically. However, it provides a direction for searching high-capacity cathode material of Na-ion batteries.

6.2 Outlook

$Na_2FeP_2O_7$ has been proven as a safe cathode and suitable for large-scale application in the Chapter 3. Chapter 4 has unveiled the ionic conducive mechanism in its crystal structure. In the future, more efforts should be concentrated on the engineering problems for further practical application.

Layered $Na[Na_{1/3}Ru_{2/3}]O_2$ delivers a significantly enhanced capacity, and indicates the participation of oxygen during the redox process. This is the first time that enhanced capacity is realized in Na-rich layered oxides although the detailed mechanism retains as a mystery. It's especially interesting that enhanced capacity could not be obtained in the disordered $Na[Na_{0.23}Ru_{0.77}]O_2$ but be "switched on" in the ordered $Na[Na_{1/3}Ru_{2/3}]O_2$. This distinguished difference supplies an opportunity to search the key hint to enhance the capacity and further improve Na-ion battery investigation.

In the future, the precise information on crystal structure change during the redox process should be pursued. Those data will give the base for convincing mechanism exploration. Powder XRD, single crystal XRD and TEM et al. are the powerful technologies for this aim. In parallel, the oxygen participation should be confirmed experimentally even it has been widely accepted theoretically as a charge compensation

to the battery redox reaction. The valence change of O as well as of the transition metal Ru should be investigated during the whole battery charge/discharge process. XAS, XPS and Mössbauer spectroscopy are among the most efficient solutions.

Acknowledgements

I would like to express my deepest appreciation to my advisor, Professor Atsuo Yamada. Without his careful guidance and wonderful suggestions, the dissertation work would never be possible. I would also like to thank Professor Hanshen Zhou, National Institute of Advanced Industrial Science and Technology (AIST), for his enlightening comments in the laboratory seminar.

I would like to thank our Associate Professor Masashi Okubo for his careful and zealous directions. I also hope give thanks to our Assistant Professor Yuki Yamada for his kind support in lab life.

I especially want to thank Dr. Shinichi Nishimura for his kind and powerful guidance in detailed experiments, I have learnt a lot during my Ph.D. study. I also want to express my thanks to Dr. Sai-cheong Chung for his patience to my puzzle and the always cheer-up discussions.

I would like to give my honest thanks to Dr. Prabeer Barpanda, an alumnus from YAMADA lab and now being an Assistant Professor in Indian Institute of Science Bangalore (IIS). He has taught me many necessary skills to be a qualified Ph.D. during our cooperation.

I would like to express my gratitude to all the members in YAMADA lab. Thanks for their kindness and the enjoyable lab life.

I want to appreciate the kind supports from all my collaborators. Professor Masatomo Yashima and Assistant Professor Kotaro Fujii in Tokyo Institute of Technology have given supports to the high temperature Synchrotron XRD experiments and provided many valuable suggestions; Associate Professor Chris D. Ling and Mrs.

Zakiah Mohamed in University of Sydney, Dr. Maxim Avdeev in Australian Nuclear Science and Technology Organization, have supplied the state data to organize the publications. Thanks to their cooperation, I can finish this dissertation.

I would like to express appreciations to the dissertation committee members, Professor Kazunari Domen, Professor Koichi Yamashita, Professor Masaru Miyayama and Associate Professor Ryuji Kikuchi, for their kind attentions and wonderful comments on my dissertation.

Most of all, I thank my family for their endless support and encouragement during my PH.D. study.

Jan. 2015

Guandong Liu